Magnetohydrodynamical Simulations of the Fragmentation of Molecular Cloud Cores

by

Logan Francis

A THESIS SUBMITTED IN PARTIAL FULFILMENT OF
THE REQUIREMENTS FOR THE DEGREE OF

BACHELOR OF SCIENCE

in

Honours Physics

(Department of Astronomy and Physics, Dr. David A. Clarke supervising faculty)

.....
.....
.....
.....
.....

SAINT MARY'S UNIVERSITY

April 11, 2014

Abstract

Magnetohydrodynamical Simulations of the Fragmentation of Molecular Cloud Cores

by *Logan Francis*

submitted on March 28, 2014:

Multiple star systems are quite common throughout the universe, so it is of interest to know what physical process may promote and prevent the *fragmentation* of a collapsing gas cloud that leads to multiple star system formation. Protostars, condensed objects in which nuclear reactions have yet to begin, are predominantly formed in *Molecular Cloud Cores*, dense regions of Molecular clouds composed of mostly cold molecular hydrogen. The condition for fragmentation is described by the *Jeans Length*, the maximm radius a uniform spherical core can have, beyond which thermal pressure is insufficient to support the core against gravitational collapse.

To simulate the formation of multiple star systems, a model was developed consisting of a sphere of uniform density with an azimuthal density perturbation to stimulate fragmentation, with some initial amount of rotation and a uniform magnetic field parallel to the rotation axis. The parameters tested were the ratios of the initial thermal, rotational, and magnetic energy to the gravitational potential energy of the sphere, and the ratio of specific heats, denoted by α, β, ζ_m and γ respectively. An α-β-ζ_m-γ parameter space survey was carried out using the magnetohydrodynamical computer code *ZEUS-3D*, augmented with a Fourier transform based gravity solver.

The increase of the energy ratios α, β, and ζ_m was found to generally provide more support against the collapse and result in the evolution of the cores to a lower density. Multiple dense fragments were produced primarily in the hydrodynamica simulations using adiabatic values of γ. The addition of a magnetic field was found to homogenize the density distribution, supress fragmentation, and prevent the movement of fluid perpendicular to field lines, resulting in a smaller collapsed core. Simulations using near-isothermal values of γ were found to generally collapse to a higher density state than those with adiabatic values, and to produce a single central condensation rather than multiple fragments.

Contents

List of Figures

Chapter 1

Introduction

Multiple star systems, consisting of two or more stars revolving around a common barycentre, are quite common throughout the universe. In the Milky Way, roughly one third of stars (Lada, 2006) and about two-thirds of G type stars like the sun (Duquennoy and Mayor, 1991) are in fact thought to be multiple star systems. Given their prevalence, it is of interest to know what physical processes may promote and prevent the *fragmentation* of a collapsing gas cloud that leads to multiple star system formation. To discuss fragmentation, a general review of star formation is warranted.

1.1 The Hierarchy of Star Forming Structures in Galaxies

The formation of stars occurs in the *interstellar medium* (ISM). The ISM contains a hierarchy of progressively denser structures which allow for the birth of stars, shown in figure 1.1. The ISM is composed of 70.4% Hydrogen, 28.1% Helium, and 1.5% metals (which in astronomy, are any elements heavier than Helium) by mass (Ferrière, 2001). It consists of three gas phases in pressure equilibrium: the hot ionized medium (HIM) (temperature T $\sim 10^6$ K; occupies a fractional volume of the ISM denoted by its *filling factor* of $f_{\rm HIM} \sim 0.7 - 0.8$), a low density ionized gas which fills the majority of the

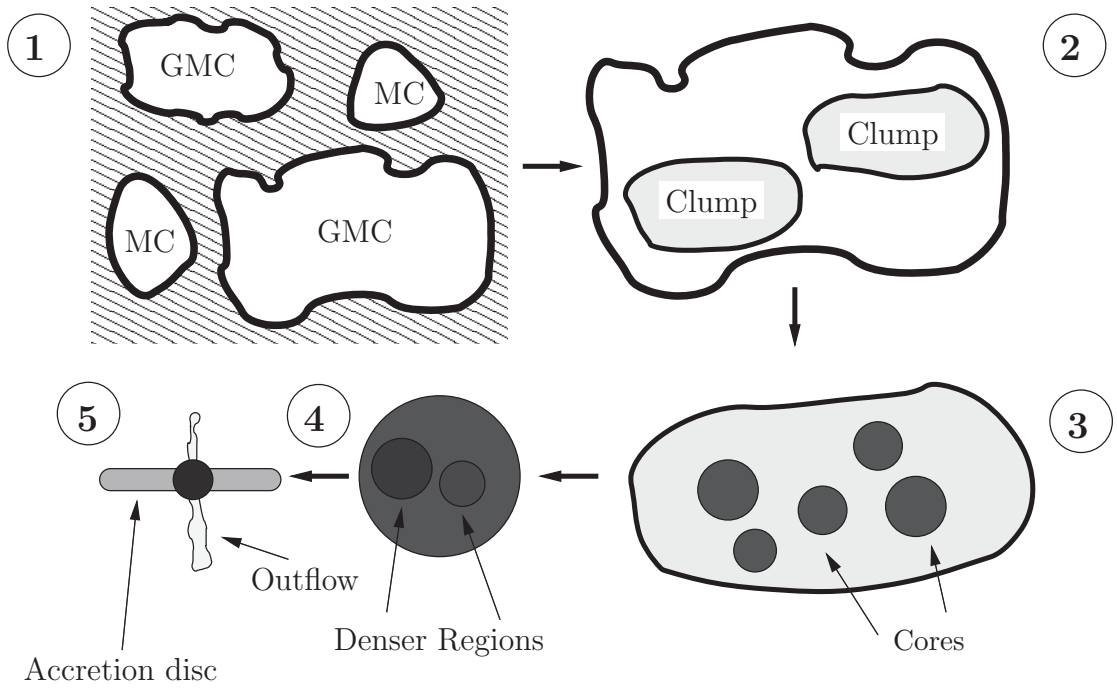

1) Interstellar Medium

- Consists of three gases in pressure equilibrium (HIM, CNM, WNM/WIM)
- Embedded Molecular Clouds (MCs) and Giant Molecular Clouds (GMCs)

2) Giant Molecular Cloud

- Dense cloud of mostly neutral molecular hydrogen and the site of most star formation.
- Sizes, masses and temperatures of $\sim 10^1 - 10^2$ pc, $10^5 - 10^6 \mathrm{M}_\odot$, $T \sim 10 - 20$ K

3) Clump

- A denser region of a molecular cloud from which an entire star cluster forms.
- Sizes, masses and temperatures of $\sim 0.3 - 3$ pc, $1 - 10^3 \mathrm{M}_\odot$, $T \sim 10$ K

4) Core

- A region in a clump which undergoes gravitational collapse to form a star system.
- Sizes, masses and temperatures of $\sim 0.01 - 0.1$ pc, $\sim 1 \mathrm{M}_\odot$, $T \sim 10$ K

5) Protostar

- The pre-nuclear first stage of a star's evolution.
- Exhibits an accretion disc and collimated outflows of gas known as *jets*.

Figure 1.1: Hierarchy of star forming structures in the ISM.

ISM, the cold neutral medium (CNM) ($T \sim 10 - 20$ K, $f_{\rm CNM} \sim 0.02 - 0.04$) which consists of mostly dense neutral and molecular gas, and a warm medium ($f_{\rm warm} \sim 0.2$) which surrounds the CNM (McKee and Ostriker, 1977). The warm medium is subdivided into the inner warm neutral medium (WNM) ($T \sim 6000 - 10000$ K), which surrounds the CNM and is composed of mostly neutral gas (fractional ionization ~ 0.1), and the warm ionized medium (WIM) ($T \sim 8000$ K), a region sandwiched between the WNM and HIM of predominantly ionized gas (fractional ionization ~ 0.7) (Ferrière, 2001).

Embedded in the ISM are the aptly named *molecular clouds* (MCs) and *giant molecular clouds* (GMCs), which are composed of mostly cold molecular hydrogen. The gas in MCs and GMCs is self-gravitating, which distinguishes them from being another gas phase of the ISM (Pudritz, 2001). An example of where a GMC can be found is in the beautiful eagle nebula, as highlighted in figure 1.2. GMCs such as this contain most of the self-gravitating gas in the Milky Way, and have a range of sizes of $10 - 100$ pc, masses of $10^5 - 10^6 {\rm M}_\odot$, and temperatures of $T \sim 10 - 20$ K (Pudritz, 2001).

The process by which GMCs form is complex and not fully understood. A variety of models describe how they form from the gas of the ISM, including cloud-cloud agglomeration, Parker instabilities, and ISM turbulence. Cloud-cloud agglomeration is thought to be caused by the passages of a the spiral arm of a galaxy, which in turn causes the collision and agglomeration of tenuous clouds into denser GMCs (Kwan and Valdes, 1983), while a magnetic field aligned with the plane of the Milky Way could create a Parker instability that produces molecular clouds (Elmegreen, 1982).

Finally, the effects of turbulence in the ISM could assist in the formation of GMCs, the details of which are beyond the scope of this thesis but are available in an extensive review of star formation by McKee and Ostriker (2007).

Another region of star formation may be *Bok globules*, low temperature ($T \sim 10$ K) clouds located outside GMCs with masses of 1–1000 $M_\odot$ and size less than 1 pc (Carroll and Ostlie, 2007). Bok Globules are thought to be star forming regions; a radio telescope survey by Launhardt et al. (2000) of 25 Bok Globules found that 40% contained condensed regions associated with newborn stars.

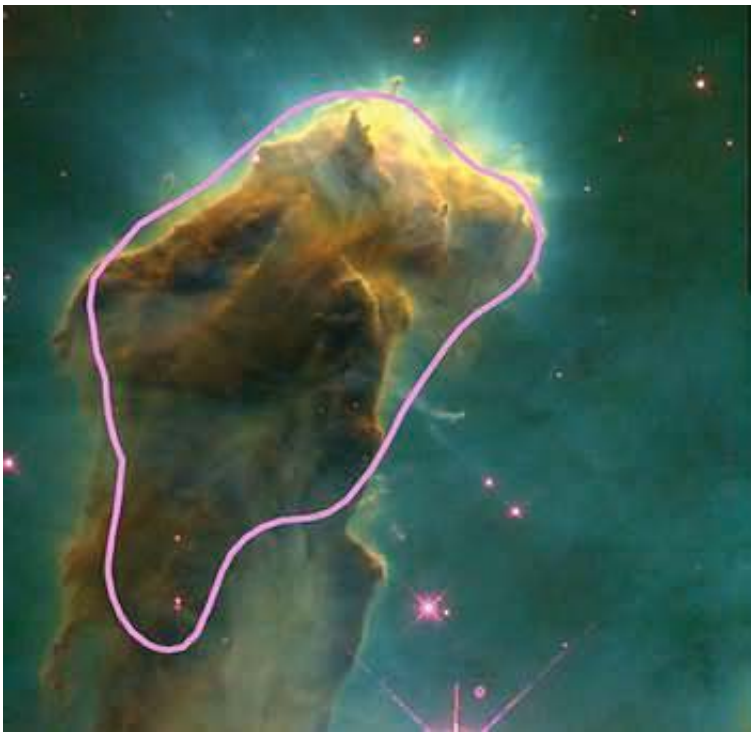

Figure 1.2: Visible light Hubble Space Telescope image of the eagle nebula. The giant molecular cloud is within the outlined region (Credit: Radio contour - Leo Blitz (UCB), image - Jeff Hester & Paul Scowen (ASU)). Since molecular hydrogen does not have any absorption or emission lines in the visible spectrum, its presence is identified by radio telescope surveys of tracer molecules (e.g., CO) associated with it (Carroll and Ostlie, 2007).

Within GMCs are denser *clumps*, from which an entire star cluster is produced.

A survey of clumps by Williams et al. (1995) in the Rosette MC found sizes to be $\sim 0.3 - 3$ pc, while masses and temperatures are generally $1 - 10^3 M_\odot$ and ~ 10 K. Clumps can form within GMCs in ways very similar to how GMCs form in the ISM, such as by clump-clump agglomeration and MHD turbulence, or by the fragmentation of magnetized filamentary clouds (Pudritz, 2001).

At an even smaller scale within clumps are *molecular cloud cores*, from which a single or multiple star system forms. Cores have sizes of $\sim 0.01 - 0.1$ pc, masses of $\sim 1 M_\odot$ (Pudritz, 2001), and temperatures of ~ 10 K (Carroll and Ostlie, 2007). Possible mechanisms for how cores form from their parent clumps include ambipolar diffusion, MHD wave damping, and cooling flows. Ambipolar diffusion in astrophysics is the gradual process by which the support a magnetic field provides a gas against gravitational collapse is removed. The magnetic field is coupled only with the ionized particles in the gas, so the motion of the neutral particles which are not directly influenced by the Lorentz force will cause the magnetic field lines to slip out of denser regions of the cloud and allow further collapse. MHD waves can provide some support for a partially ionized gas, but have been shown to be damped at approximately the scale of cores (Pudritz, 2001). This damping can cause a pressure imbalance that in turn causes material to flow into and cool a region of lower pressure, increasing its density and allowing for the formation of a core.

Finally, the smallest scale of interest is the *protostar*. A protostar is a condensed object in which nuclear reactions have yet to begin and is the earliest stage of stellar evolution. Protostars typically exhibit a rotating accretion disc and jets: collimated streams of supersonic plasma launched from the protostar. Both jets and an accretion

disc can be seen in the image of the protostar in HH-30 shown in figure 1.3. The jets provide a way for gas in the accretion disc to shed excess angular momentum that would normally prevent further collapse. Collapsing ionized gas is launched outward along magnetic field lines aligned with the rotation axis of the accretion disc, shedding much of its angular momentum and allowing it to fall inwards on to the protostar (e.g. Clarke et al., 2008).

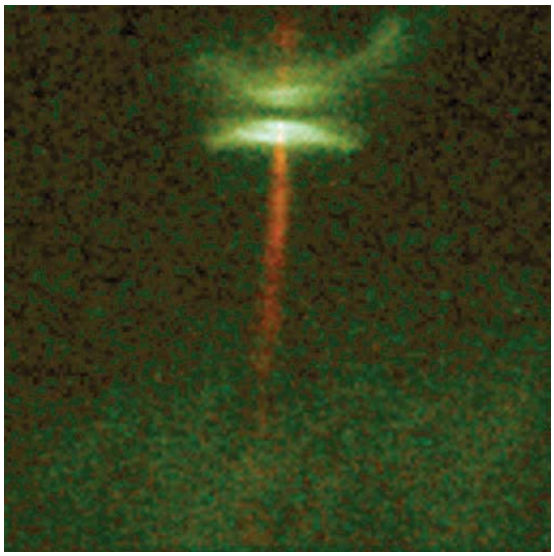

Figure 1.3: Visible light Hubble Space Telescope image of the Herbig-Haro object HH-30 (Credit: C. Burrows (STScI & ESA), the WFPC 2 Investigation Definition Team, and NASA). A jet is seen emanating from top to bottom, its source is the protostar hidden by the accretion disc.

1.2 The Physics of Collapse and Fragmentation of Molecular Cloud Cores

Simple analytical models for the conditions necessary for a spherical core to collapse were first derived by the astrophysicist James Jeans in 1902 using the *virial theorem*.

The virial theorem (Carroll and Ostlie, 2007)

$$2\langle K\rangle + \langle U\rangle = 0 \tag{1.1}$$

represents the equilibrium condition of a system with average internal kinetic (i.e., thermal) energy $\langle K\rangle$, and an average energy of a central potential $\langle U\rangle$. It may be extended to include the effects of external pressures, magnetic fields, rotation and more, but Jeans' original analysis only considered the quantities in equation (1.1). Simply put, the virial theorem requires that if the core is to collapse, then its kinetic energy must be less than half its potential energy. For a core modelled as a sphere of ideal gas of volume V, radius R, uniform density ρ_0, mass M, and temperature T, the thermal energy and gravitational potential energy are given as:

$$E_{\text{th.}} = \frac{3MkT}{2\mu m_{\text{H}}}, \tag{1.2}$$

and,

$$U_{\text{grav.}} = \frac{3GM^2}{5R}, \tag{1.3}$$

respectively, where k is the Boltzmann constant, μ is the mean molecular weight, and m_{H} is the mass of a hydrogen atom. When substituted into (1.1), the condition for collapse can be manipulated to produce:

$$M > M_{\text{J}}\ ,\ M_{\text{J}} = \left(\frac{5kT}{G\mu m_{\text{H}}}\right)^{3/2}\left(\frac{3}{4\pi\rho_0}\right)^{1/2}; \tag{1.4}$$

$$R > \lambda_{\rm J} \ , \ \lambda_{\rm J} = \left(\frac{15kT}{4\pi G \mu m_{\rm H} \rho_0} \right)^{1/2} , \tag{1.5}$$

where $M_{\rm J}$ and $\lambda_{\rm J}$ are known as the *Jeans mass* and *Jeans length* respectively. A gas cloud with a mass or radius larger than the corresponding Jeans mass or length will collapse under its own gravity. Alternatively, the Jeans length can be derived from the equations of ideal hydrodynamics using perturbation analysis (McMillan, 2014);

$$\lambda_{\rm J} = \left(\frac{\pi c_{\rm s}^2}{G\rho} \right)^{1/2} , \tag{1.6}$$

where $c_{\rm s}$ is the isothermal ($c_{\rm s} = (p/\rho)^{1/2}$) or adiabatic ($c_{\rm s} = (\gamma p/\rho)^{1/2}$) sound speed. For an isolated core with mass larger than the Jeans mass undergoing an isothermal collapse, the Jeans quantities depend only upon the density. Hence, as gravitational collapse proceeds, the density of the cloud will increase, lowering the Jeans mass and causing the collapse to continue in a runaway fashion.

However, the collapse of the core is only isothermal provided the cloud is optically thin so that the gravitational potential energy can be radiated away (Carroll and Ostlie, 2007). As the density of the cloud increases, so does the optical thickness, causing the collapse to be more adiabatic in nature. A rise in temperature of the core and *increase* of the Jeans quantities ensues. When the core becomes hot enough, thermal pressure will support the core against further gravitational collapse, and a new virial equilibrium state will be achieved.

During the adiabatic portion of the collapse, the degrees of freedom of the gas molecule affects how the thermal energy changes as a function of density. Using the

ideal gas law in the form, $p = (\gamma - 1)e$, where p, γ, and e are the pressure, ratio of specific heats, and internal energy density respectively, the thermal energy can also be written as:

$$E_{\text{th.}} = eV = \frac{pM}{(\gamma - 1)\rho_0}. \tag{1.7}$$

With the substitution of the adiabatic relationship between pressure and density, $p \propto \rho_0^{\gamma}$, it is then clear that

$$E_{\text{th.}} \propto \rho_0^{(\gamma-1)} \tag{1.8}$$

provided that the core is not accreting a significant amount of mass so that M is approximately constant. Comparing this to the analogous relationship for $U_{\text{grav.}}$:

$$U_{\text{grav.}} \propto \rho_0^{1/3}, \tag{1.9}$$

it can be seen that for $\gamma > 4/3$, as is the case for a monatomic ($\gamma = 5/3$, e.g. atomic hydrogen) or diatomic gas ($\gamma = 7/3$, e.g. molecular hydrogen), the thermal energy of the core increases faster with increasing density than the gravitational energy. For γ less than the critical 4/3, approximating an isothermal ($\gamma = 1$) or near isothermal equation of state, the reverse occurs. This demonstrates why the change of the character of the equation of state from isothermal to adiabatic arrests the collapse and allows a new virial equilibrium to be established.

Other non-thermal effects also play a role in the core collapse. The rotation of a core can provide support against contraction. Consider the case of the spherical core in solid body rotation at angular speed Ω about an axis through its centre. As

the core contracts, the angular speed of its constituent particles will increase as a consequence of the conservation of angular momentum. The particles will eventually reach a critical speed, the so-called "centrifugal barrier", where they can no longer collapse inward on to the centre of the core. This inhibits collapse perpendicular to the axis of rotation, but not parallel, resulting in the flattening of the core into a more oblate and disc-like shape. The amount of rotational energy is given by:

$$E_{\text{rot.}} = \frac{MR^2\Omega^2}{5}. \tag{1.10}$$

Magnetic fields can also support the core against collapse. To demonstrate this, the virial theorem can be modified to incorporate magnetic energy (Krumholz, 2011):

$$2\langle K\rangle + \langle E_{\text{mag.}}\rangle + \langle U\rangle = 0, \tag{1.11}$$

provided that the field outside the core is negligible in comparison with that within. The magnetic energy for a spherical cloud permeated by a uniform magnetic field is:

$$E_{\text{mag.}} = \frac{B^2V}{2\mu_0} = \frac{B^2M}{2\mu_0\rho_0} = \frac{2\Phi_B^2}{\mu_0\pi R}, \tag{1.12}$$

where $\Phi_B = \pi R^2 B$ is the magnetic flux passing through the cloud. The magnetic energy increases with density at the same rate as the gravitational potential energy (equation 1.3), indicating that magnetic support does not increase as the collapse proceeds (Krumholz, 2011). The spherical cloud can only be in equilibrium provided the magnetic fields are strong enough initially, and the process of ambipolar diffusion

will tend to gradually weaken the magnetic field's supporting effect.

When equations (1.3) and (1.12) are substituted in (1.11) and thermal support is assumed to be negligible, a *magnetic critical mass* analogous to the Jeans mass can be obtained (see appendix A):

$$M_B = \left(\frac{10\Phi_B^2}{3\mu_0\pi}\right)^{1/2}. \tag{1.13}$$

A magnetically supported cloud with $M > M_B$ is said to be *magnetically supercritical* and will collapse; a core with $M < M_B$ is said to be *magnetically subcritical* and will be stable. Collapsing magnetically subcritical clouds have no hope of becoming magnetically supercritical without changes in the magnetic field, but may become stable thanks to thermal pressure.

While the above analysis neglects other physics present (e.g., turbulence) which may arrest or expedite the collapse, it is sufficient to describe the general mechanism of the fragmentation of the core which leads to the formation of multiple protostars. As the collapse proceeds, the Jeans mass may increase or decrease, depending on the competing increase of cloud temperature and density. Cores are generally not very uniform, so the mass of smaller regions of the cloud may exceed their local Jeans mass. Each of these regions will continue to collapse under their own gravity until an equilibrium state is eventually reached, or may in turn fragment themselves, as shown in figure 1.4.

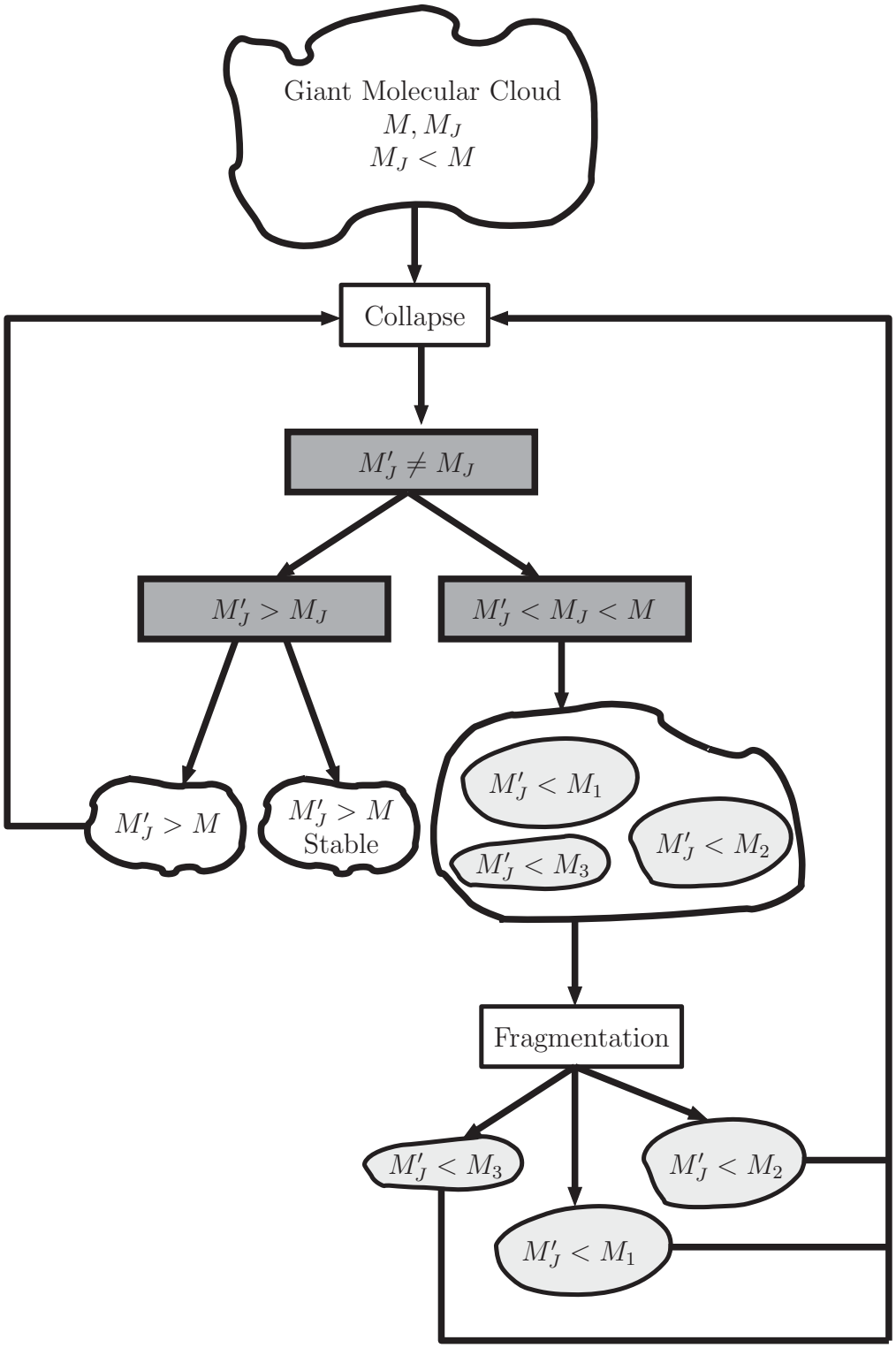

Figure 1.4: Inhomogeneity in core structure and changing Jean's mass causes fragmentation during collapse. Here, M'_J is the new Jeans mass of the cloud after it is altered by the collapse. M_1, M_2, and M_3 are the masses of the fragments which exceed the Jeans mass (recreated from Prialnik, 2000).

1.3 Modelling Core Collapse Numerically

1.3.1 Energy Ratios and Model Parameters

It is useful for the purposes of simulation to describe how collapse may be affected by the initial conditions of the spherical core in terms of ratios of various energies to the gravitational potential energy. Following the convention of Norman et al. (1980), the quantities α and β represent the gravitational energy ratios for thermal and rotational energy. Using the form of $E_{\rm th.}$ given by equation (1.7) and $\gamma = 5/3$ for a monatomic gas, α is;

$$\alpha = \frac{E_{\rm th.}}{U_{\rm grav.}} = \frac{5}{2}\left(\frac{3}{4\pi\rho_0 M^2}\right)^{1/3}\frac{c_{\rm s}^2}{G}, \tag{1.14}$$

where the isothermal sound speed $c_{\rm s}^2 = p/\rho_o$ was used. Similarly, β becomes

$$\beta = \frac{E_{\rm rot.}}{U_{\rm grav.}} = \frac{MR^2\Omega^2}{5}\frac{5R}{3GM^2} = \frac{1}{4\pi}\frac{\Omega^2}{G\rho_0}, \tag{1.15}$$

where the rotation axis points in the $\theta = 0, \phi = 0$ direction.

These ratios are commonly used to describe numerical simulations for the collapse of spherical cores, such as those by Boss (1993), Burkert and Bodenheimer (1993), and Narita et al. (1984), who investigated the values of α and β which would cause the fragmentation of the core. This thesis uses a modified version of the uniform spherical core model of Boss (1993), consisting of a uniform sphere of gas embedded in an ambient medium, where fragmentation is stimulated by an azimuthal density

perturbation of the form:

$$\rho(r) \rightarrow \rho(r)(1 + A\cos(m\phi)). \tag{1.16}$$

The modification made to this model is the addition of a uniform magnetic field, where, using (1.12), the magnetic energy ratio, ζ_m, is written as:

$$\zeta_m = \frac{E_{\text{mag.}}}{U_{\text{grav.}}} = \frac{5B^2}{6G\mu_0}\left(\frac{3}{4\pi\rho_0 M^5}\right)^{1/3}, \tag{1.17}$$

with the direction of the field denoted by the angles B_θ and B_ϕ.

In general, larger values of α, β, and ζ_m should provide additional support against gravitational collapse, while changes to γ should alter the evolution of thermal energy with increasing density, as outlined in §1.2.

1.3.2 Artificial Fragmentation and The Jeans Condition

Many of the simulations of core collapse in the 1980s and 1990s were found to be flawed by Truelove et al. (1997). An inherent cost of modelling the equations of ideal (M)HD is the introduction of finite errors to the solution for the problem. These errors can act as perturbations to regions of the simulated core, causing them to collapse if the perturbations are larger than the Jeans length. This numerical means of producing fragments which would otherwise not exist was deemed *artificial fragmentation* by Truelove et al. (1997).

However, the same paper identified a solution to the problem. By ensuring that the Jeans length is adequately resolved, the finite errors to the solution can be made small enough that artificial fragmentation does not occur. The level of resolution of the Jeans length is described by the dimensionless *Jeans Number*:

$$J_x = \Delta_x / \lambda_j, \tag{1.18}$$

where Δ_x is the resolution of a computational zone in the x direction. To ensure that artificial fragmentation does not occur, the *Jeans condition* requires only that,

$$J_x < 0.25. \tag{1.19}$$

Truelove et al. were able to accomplish this using a method known as *adaptive mesh refinement* (AMR) (Berger and Oliger, 1984; Berger and Colella, 1989), which is used by grid based computer codes that solve the equations of fluid dynamics to insert dynamically higher resolution grids (i.e., meshes) where they are needed, as visualized in figure 1.5. In the case of simulations of gravitational collapse, grids of typically twice the current level of resolution can be inserted in regions where the Jean's number reaches $J_x = 0.25$, automatically reducing Δ_x and thus, J_x.

Truelove et al. tested existing models of the isothermal collapse of spherical cores with the addition of AMR, including the Gaussian density profile used by Burkert and Bodenheimer (1993) and the uniform core model used by Boss (1993). Truelove et al. more rigorously defined a fragment as the mass contained between a local den-

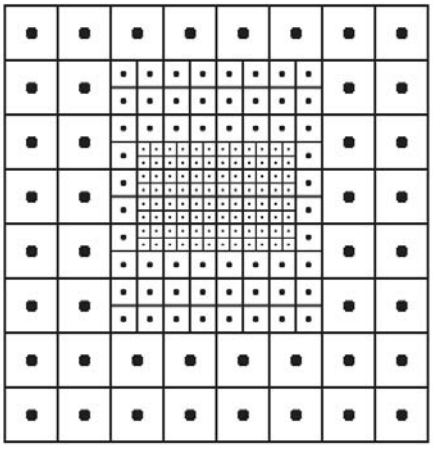

Figure 1.5: In a grid based code which uses adaptive mesh refinement, the finer resolution grids are placed where required within the coarser grid as the simulation progresses.

sity maximum and the lowest isodensity surface surrounding only that maximum, a useful definition which is adopted in this thesis (Truelove et al., 1998). For a rotating Gaussian cloud with an $A = 0.1, m = 2$ perturbation, two simulations differing only in the maximum value of J_x allowed were performed. Two fragments were produced when only $J_x < 0.5$ was enforced, while a single bar structure was produced when (1.19) was maintained, demonstrating the existence of artificial fragmentation (Truelove et al., 1997). For a uniform spherical core with $\alpha = 0.26, \beta = 0.16$ and an $A = 0.1, m = 2$ perturbation, where (1.19) was enforced, the core was observed to form two elongated fragments connected by a relatively high density bar, after the density in the simulation has been allowed to increase by 8 decades (Truelove et al., 1998).

1.4 Scope of this Thesis

As discussed, the physics of how a molecular cloud core becomes a protostar is complex, involving the effects of gravitation, radiative heating, rotation, magnetic fields, and turbulence. The focus of this thesis is on developing computer models using the staggered grid astrophysical MHD code *ZEUS-3D* (discussed further in §2.1) to examine how some of these processes affect the fragmentation of molecular cloud cores and the resulting formation of multiple protostar systems.

The model used for this investigation is the modified perturbed uniform sphere model of Boss (1993) described in §1.3.1. While this model is simple and does not include the physics of turbulence or radiative heating, it still provides the opportunity to study the effects of several parameters. In this work, the parameters α, β, ζ_m, and γ used in this model form a parameter space that is explored at a low resolution for $B_\theta = 0$ and $B_\phi = 0$.resolution studies

The difficulty in performing these core collapse simulations lies in maintaining the Jeans condition needed to ensure any fragmentation is physical. The AMR technique discussed in §1.3.2 can be used to this end. A version of the *ZEUS-3D* code equipped with AMR, AZEuS, is capable of solving the equations of ideal MHD as described by Ramsey et al. (2012). AZEuS does not yet implement an algorithm of solving the self gravity equations in less than $\mathcal{O}(N^2)$ time, i.e., the computational time for any simulation requiring gravitation will rise at least as the square of the number of points in the simulation. This makes increasing the resolution (either locally with AMR, or over the entire grid) quite impractical.

As part of this thesis, *ZEUS-3D* has been augmented with a Fourier transform based gravity solver which operates in $\mathcal{O}(N \log_2 N)$ time, described in §2.2. Since the resolution used by *ZEUS-3D* can not be changed during the simulation, this is not as desirable as an AMR compatible $\mathcal{O}(N \log_2 N)$ gravity solved implemented in AZEuS. However, the Fourier transform algorithm is useful as a bridge to performing such calculations, since it may eventually be adapted for AZEuS.

In the absence of AMR, it is not possible to maintain the Jeans condition by increasing the resolution dynamically. Instead, the Jeans number in each computational zone must be calculated at each time step of the simulation, with the maximum of these Jeans numbers ensured to be less than the value of 0.25 required by the Jeans condition. A subroutine to perform this task has been added to *ZEUS-3D*, as described in §2.3.

Furthermore, without AMR, the scale that the collapse can be followed to is much more limited, as the rise in density of the core tends to quickly violate the Jeans condition. This makes it difficult to model cores with less thermal, magnetic, or rotational support against gravitational collapse. Despite this, fragmentation and other questions can still be investigated within the Jeans condition compliant $(\alpha, \beta, \zeta_m, \gamma)$ parameter space.

A situation that can be considered is that of a perturbed isothermal core without a magnetic field and a low value of α. Collapse for this core should proceed in a runaway fashion, as explained in §1.2. By increasing only the value ζ_m, this core should instead collapse to an equilibrium state. With the introduction of rotation, the core may fragment into two magnetically supercritical cores. In reality, these

cores might gradually lose magnetic support by the effects of ambipolar diffusion, and eventually collapse, allowing the formation of a binary system.

For rotating non-isothermal cores, lower values of ζ_m and α should be needed to provide support for the collapsing core. The effects of less initial thermal and magnetic support versus making a collapse more adiabatic in nature on the fragmentation of the core can be examined as well.

The effect γ may have on fragmentation can also be explored. Since lower values of γ result in a slower increase of thermal energy with density, the effect of larger values of γ will likely be the suppression of fragmentation.

Chapter 2

Numerical Methods

2.1 MHD and *ZEUS-3D*

ZEUS-3D is a grid based MHD code designed for astrophysical applications. It makes use of a staggered mesh where scalar quantities are located at the centre of a computational zone (i.e, one "box" on the defined grid), while components of vector quantities are found at their respective faces. *ZEUS-3D* solves the equations of ideal hydrodynamics in a variety of dimensions $(1, 1\frac{1}{2}, 2, 2\frac{1}{2}, 3)$ and coordinate systems (Cartesian, cylindrical, spherical), with options to incorporate various physics beyond the basic hydrodynamics, such as magnetic fields, self-gravity, viscosity, two fluids, and more (Clarke, 1996, 2010). For the purposes of this work, the equations solved are:

$$\frac{\partial \rho}{\partial t} + \nabla \cdot (\rho \vec{v}) = 0, \qquad \text{continuity,} \tag{2.1}$$

$$\frac{\partial \vec{s}}{\partial t} + \nabla \cdot (\vec{s}\vec{v} + (p + p_B)\mathbf{1} - \vec{B}\vec{B}) = -\rho \nabla \phi, \qquad \text{momentum,} \tag{2.2}$$

$$\frac{\partial e_T}{\partial t} + \nabla \cdot \left[(e_T + p - p_B)\vec{v} + \vec{E} \times \vec{B} \right] = 0, \qquad \text{total energy,} \tag{2.3}$$

$$\frac{\partial \vec{B}}{\partial t} = \nabla \times (\vec{v} \times \vec{B}), \qquad \text{induction.} \tag{2.4}$$

where:

ρ	is the matter density;
$\vec{v}$	is the velocity;
p	is the thermal pressure;
p_B	is the magnetic pressure $= \frac{1}{2}B^2$;
$\mathsf{1}$	is the unit tensor;
$\vec{B}$	is the magnetic induction, in units where $\mu_0 = 1$;
ϕ	is the gravitational potential, in units where $G = \frac{1}{4\pi}$;
e	is the internal energy density;
e_T	is the total energy density $= e + \frac{1}{2}\rho v^2 + \frac{1}{2}B^2 + \phi$.

All simulations in this work use *ZEUS-3D* in a 3-D mode with a Cartesian geometry, including the extra physics of magnetic fields and self-gravity, and solving the total energy equation. The total energy equation (2.3) is used because it provides strict conservation of e_T. However, the total energy equation does not guarantee positive definite e, which affects the calculation of the Jeans number as discussed in §2.3.

2.2 Solving Poisson's Equation for Gravity

Poisson's equation for gravity (referred to hereafter as "Poisson's Equation") is given by:

$$\nabla^2\phi = 4\pi G\rho, \qquad \text{where } G = \frac{1}{4\pi} \text{ in } \textit{ZEUS-3D}, \tag{2.5}$$

is an elliptical partial differential equation which can be used to find the gravitational potential ϕ associated with a density distribution ρ of an object such as a core in a molecular cloud. Consider the 1-D case of

$$\frac{\partial^2}{\partial x^2}\phi(x) = \rho(x). \tag{2.6}$$

This can be solved for ϕ by performing a Fourier transform on ϕ and ρ. For some general function $h(t)$, we have:

$$\hat{h}(f) = \mathcal{F}[h(t)] = \int_{-\infty}^{\infty} h(t)e^{2\pi ift}dt, \qquad \text{the forward Fourier transform;} \tag{2.7}$$

$$h(t) = \mathcal{F}^{-1}[\hat{h}(f)] = \int_{-\infty}^{\infty} \hat{h}(f)e^{-2\pi ift}df, \qquad \text{the inverse Fourier transform.} \tag{2.8}$$

The function $\hat{h}(f)$ is said to be in *Fourier space*, and the exponential terms in the forward and inverse transforms are respectively known as their *kernel* and *inverse kernel*; functions which define any integral transform.

The Fourier transform has the useful property:

$$\mathcal{F}\left[\frac{d}{dt}h(t)\right] = (-2\pi i f)\hat{h}(f), \tag{2.9}$$

which allows Poisson's equation to be solved by the following method:

1. Take the Fourier transform of Poisson's equation.
2. Solve the resulting algebraic equation in Fourier space for $\hat{\phi}$
3. Take the inverse Fourier transform of $\hat{\phi}$ to obtain ϕ.

For this work, a gravity solver based on this method and as described by Press et al. (1992) has been implemented in *ZEUS-3D*. In *ZEUS-3D*, ϕ and ρ are both discrete, zone centred quantities, and a *discrete Fourier transform* (DFT) pair takes the form:

$$\hat{h}_n = \sum_{k=0}^{N-1} h_k e^{2\pi i k n/N}, \qquad \text{the forward DFT;} \tag{2.10}$$

$$h_k = \frac{1}{N}\sum_{n=0}^{N-1} h_n e^{-2\pi i k n/N}, \qquad \text{the inverse DFT;} \tag{2.11}$$

where N is the number of points in the transform. The DFT is used to solve Poisson's equation numerically in a way analogous to the 1-D continuous case. This is easily generalized to 1, 2, or 3 Cartesian dimensions, using either a multidimensional DFT, or, as is the case for the *ZEUS-3D* gravity solver, repeated application of the one dimensional DFT.

Although simple, the kernel of this type of DFT imposes periodic boundary conditions on the solution for ϕ obtained. If zero (Dirichlet) boundary conditions are

desired instead, a sine wave kernel can be used to create a discrete sine transform (DST):

$$\hat{h}_n = \sum_{k=1}^{N-1} h_k \sin(\pi k n/N). \tag{2.12}$$

Interestingly, the DST is its own inverse but for a constant, and is used in a manner analogous to the DFT to solve Poisson's equation.

If inhomogeneous boundary conditions are desired, the density distribution is first modified by the boundaries needed for ϕ, and ϕ is then solved for in the same way as the zero boundary condition case. The details of this modification and the method used to solve Poisson's equation are available in appendix B.

While the DFT and DST provide a straightforward way to solve Poisson's equation, computing them directly is not efficient. To calculate the DFT requires N multiplications for each of the N points in the transform, and so the DFT is said to be an $\mathcal{O}(N^2)$ algorithm. Similarly, a DST would require at least $\mathcal{O}(N(N-1))$ calculations. An algorithm known as the *Fast Fourier Transform* (FFT) (Cooley and Tukey, 1965; following Danielson and Lanczos, 1942) circumvents this problem by taking advantage of a degree of freedom one has in the order in which the arithmetical operations are made, rendering it an $\mathcal{O}(N \log_2 N)$ algorithm. Despite this significant speed improvement, the result of the FFT is identical to that of the DFT to within machine round off error, and hence it is the most common algorithm used to perform the DFT. A similar $\mathcal{O}(N \log_2 N)$ *Fast Sine Transform* (FST) algorithm also exists; it and the FFT algorithm used in this work can be found in Press et al. (1992).

The only downside to the use of the FFT or FST algorithms implemented is

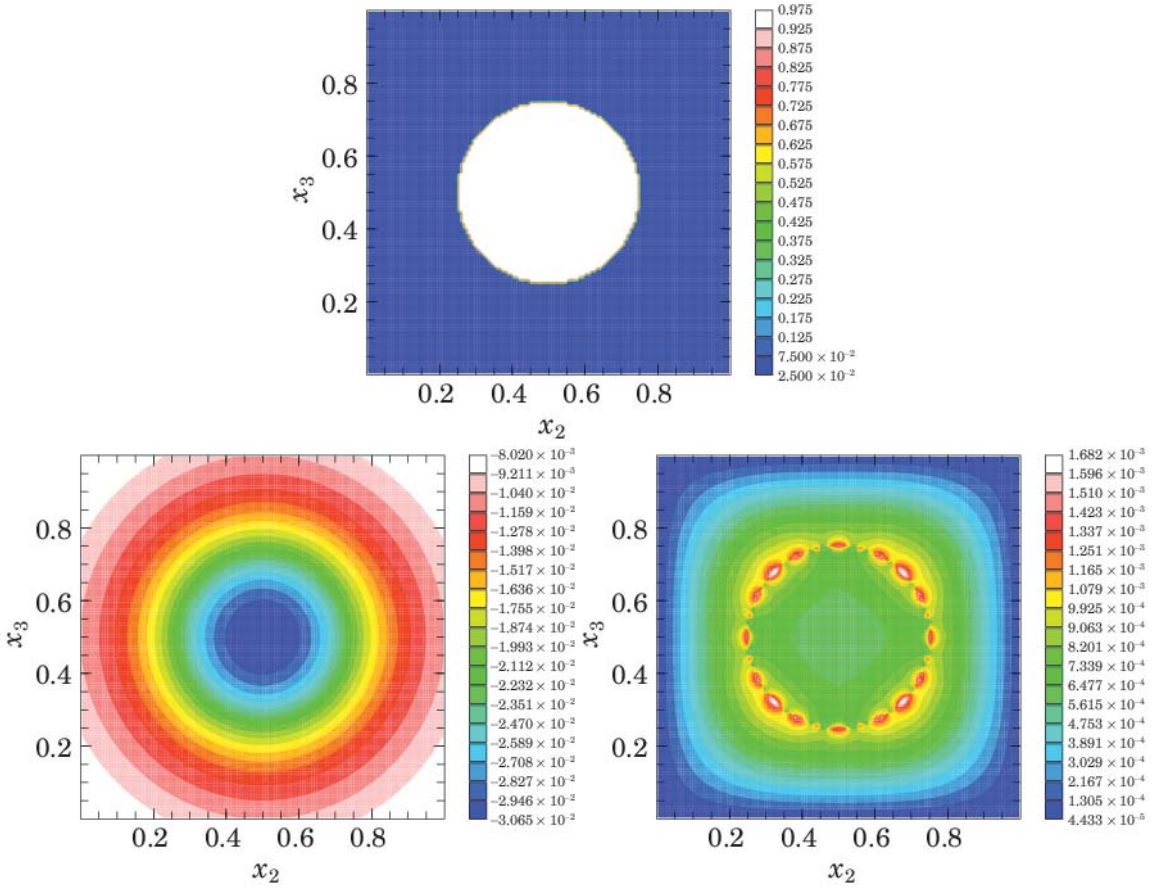

Figure 2.1: Counterclockwise from top: Equatorial slices through a uniform sphere of the density, gravitation potential computed by the FST, and relative error of the FST gravitational potential relative to the known solution The error in the solution ($\sim 0.1\%$) is greatest at the sharp drop in density at the sphere's surface.

a restriction on the size of the grid used. The number of active zones (zones which change as the calculation progresses, enclosed by boundary zones), n, in any dimension any dimension must be 2^n for the FFT (periodic boundaries), and $2^n - 1$ for the FST (zero or inhomogeneous boundaries).

To test the gravity solver installed in *ZEUS-3D*, analytical solutions to Poisson's equation for a variety of density distributions are compared with those computed by FFT and FST. The results for the FST solver with a uniform sphere are shown in figure 2.1.

2.3 Monitoring the Jeans Condition

For numerical purposes, the Jeans length in the form given by equation (1.6) is typically used. Since (1.6) depends on the sound speed, the value of γ affects the calculation of the Jeans length. For an isothermal ($\gamma = 1$) simulation, the relationship $p \propto \rho$, would cause the sound speed to be constant throughout the grid, and the Jeans length to depend only on density. However, because the simulations performed in this work only use adiabatic ($\gamma = 4/3, 5/3$) or approximately isothermal ($\gamma = 1.001$) values of γ, and because the total energy equation (2.3) is solved, $c_{\rm s}$ can vary from point to point.

To determine if the Jeans condition is violated by a simulation, the maximum Jeans numbers are calculated by the following procedure:

1. Calculate the square of the adiabatic sound speed by $c_{\rm s}^2 = \dfrac{\gamma(\gamma-1)e}{\rho}$ for every point on the grid.

2. Calculate $\lambda_{\rm J}$ by equation 1.6

3. Calculate J_x by equation 1.18.

4. Determine the maximum J_x on the grid.

5. Record the maximum J_x, and relevant associated quantities.

6. Advance the simulation another step and repeat.

where it should be noted that only J_x need be calculated for a Cartesian simulation on a uniformly resolved grid where $\Delta_x = \Delta_y = \Delta_z$. A side effect of the use of the

total energy equation is that e, the internal energy density, is not necessarily positive definite. Since this is non-physical, *ZEUS-3D* resets these points to the smallest positive number available on the machine. This renders the sound speeds and in turn the Jeans numbers at these locations non-physical as well. To prevent these non-physical Jeans numbers from being reported as the maximum, any Jeans numbers calculated in step 3 using $c_s^2 = 10^{-10}$ are set to zero.

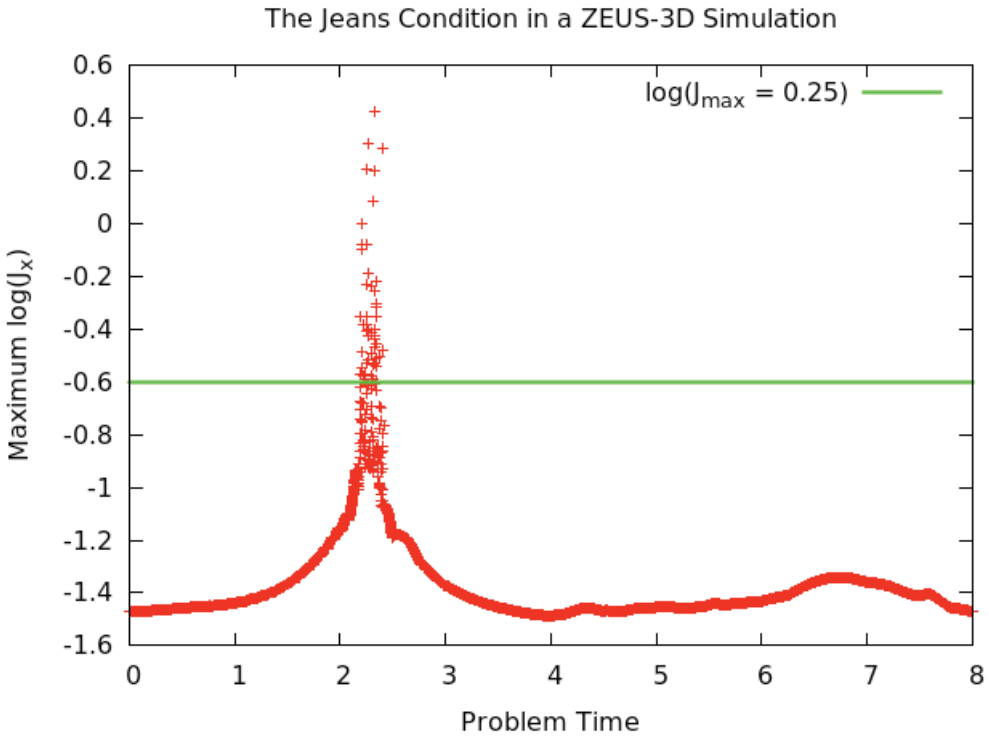

Figure 2.2: A *ZEUS-3D* simulation of a collapsing core where the Jeans condition is violated at $\approx t = 2.2$

By plotting the maximum J_x against the problem time or time step, it is easy to tell when the Jeans condition (equation 1.19) is violated, as shown in 2.2. Plots of this type and scripts which analyze the data files are used to ensure that no simulations which violate the Jeans condition are considered for analysis.

2.4 Collapsing Core Model Setup

The numerical model for a molecular cloud core used is based on those used by Boss (1993) and Truelove et al. (1998). All simulations are performed in 3-D using Cartesian geometry on a grid with an equal number of zones (127) in each direction. Position on the grid is measured by the perpendicular x, y, and z (referred to in *ZEUS-3D* as x_1, x_2, and x_3 respectively) axes, which all range from $0.0 - 1.0$. The equations solved are equations (2.1), (2.2), (2.3), (2.4), and (2.5).

Without any perturbation, the initial setup consists of a sphere of gas of uniform density $\rho_0 = 1$ and initial radius $r_0 = 0.25$, embedded in an ambient medium with a uniform density of $\rho_{\rm amb} = 0.01$, in pressure equilibrium. To stimulate fragmentation, an $A = 0.1$, $m = 2$ density perturbation of the form described by (1.16) is applied. A plot produced by *ZEUS-3D* of a slice through the middle of the sphere and perpendicular to the rotation axis (z) is shown in figure 2.3 to demonstrate the structure of the perturbation.

The hydrodynamical boundary conditions used are outflow, that is, any material which strikes a boundary exits the grid. This could interfere with the calculation of the gravitational potential, but the space between the sphere and the boundary ensures that a significant amount of mass can escape only if the core expands greatly.

The gravitational potential boundary conditions used are inhomogeneous, requiring the use of the FST based Poisson solver, which restricts the number of active zones which span the grid to $2^n - 1$. These boundaries are calculated analytically as those of the potential of a uniform sphere, and remain constant throughout the simu-

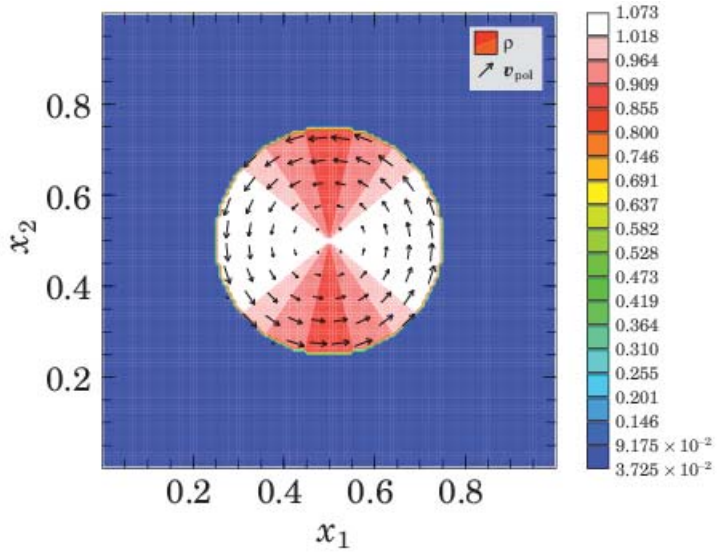

Figure 2.3: An equatorial slice of the initial density of the uniform sphere in *ZEUS-3D*. The overlaid velocity vectors show the initial rotation of the sphere.

lation. Given that the sphere is initially separated from the boundaries by a distance equal to its radius, and that the sphere collapses towards the centre and away from the boundaries, static boundary conditions should not be unrealistic.

The energy ratio α is used to set the initial thermal energy of the sphere. The ratio β is used to set the initial velocity of all of the points within the sphere, so as to produce a solid body rotation. The ratio ζ_m is is used to set the strength of the uniform magnetic field, which by default is aligned along the rotation axis.

The ratio of specific heats γ used remains constant throughout the simulation, and is one of 1.001, 4/3, or 5/3. Together with the energy ratios and the alignment of the magnetic fields, these quantities form the parameter space which is explored in this work to examine their effects on fragmentation.

Finally, the amount of time during which the simulation is allowed to run is

described in terms of the free fall time,

$$t_{\rm ff} = \left(\frac{3\pi}{32 G \rho_0} \right)^{1/2}. \tag{2.13}$$

The free-fall time is the time a uniform sphere with no supporting pressure would take to collapse to a singularity under its own gravity. For the simulations explored, $t_{\rm ff} \approx 2$, and the simulations are allowed to evolve until a problem time of $t = 8.0$, about 4 free-fall times.

Chapter 3

Discussion of Simulations

The effect of the energy ratios α, β, and ζ_m and the ratio of specific heats on the fragmentation and morphology of collapsing molecular cloud cores discussed in §1.2 and §1.3.1 was explored by the parameter space survey shown in table 3.1. All simulations in this survey use 127 active zones in each direction, with the numerical setup for a perturbed uniform spherical core explained in §2.4. The presence of fragments is evaluated using the definition of a fragment provided in §1.3.2.

Table 3.1: Parameter space explored at 127^3 resolution. All combinations of the parameters are tested, for a total of 432 simulations.

α	β	ζ_m	γ
0.2	0.0	0.0	1.001
0.4	0.1	0.5	4/3
0.6	0.2	1.0	5/3
0.8	0.3	2.0	
1.0	0.4		
1.2	0.5		

Figures 3.3 to 3.12 depict the end of all simulations with $\zeta_m = 0.0$ and with a ζ_m chosen to best represent results for a particular γ (otherwise identical simulations with $\zeta_m = 0.5, 1.0$, and 2.0 were qualitatively very similar) using α–β planes of the parameter space. Each image in all of these figures depicts the density in a slice through the middle of the grid perpendicular or parallel to the axis of rotation (z) at the end of the simulation (problem time $t = 8.0$), with the parameters specified.

Blank spaces in the plots correspond to simulations which violated the Jeans condition (equation 1.19). All simulations exhibit 180° rotational symmetry because of the $m = 2$ perturbation mode and the use of a Cartesian grid.

3.1 Hydrodynamical Simulations

Depicted in figures 3.1 to 3.6 are equatorial and rotation axis slices of hydrodynamical simulations for $\gamma = 5/3, 4/3$ and 1.001 respectively.

The prevalent effect of a larger α for all simulations is the evolution of the core to a state of lower density. An exception is seen for the ($\alpha = 0.2-1.2, \beta = 0.3-0.5, \zeta_m = 0.0, \gamma = 4/3$) region of the parameter space, displayed in the top three rows of figures 3.3 and 3.4. Here, $\alpha > 1.0$ results in a condensation in the centre of the core. The general effect of increased β is the widening of the diameter of the end state core perpendicular to the rotation axis and a transition from an oblate spheroidal to a disc shaped structure, sometimes exhibiting a bulge.

The structure of the core at simulation end depends greatly on the ratio of specific heats, γ. For the $\gamma = 5/3$ case, a few different classes of shapes emerge, displayed in figures 3.1 and 3.2. With no rotation, collapse proceeds to form an oblate spheroid containing two denser central regions formed from the perturbation, which have larger densities and smaller separations for lower α. Of these, the $\alpha = 0.2$ simulation has a single fragment, the $\alpha = 0.4, 0.6$ simulations show two condensed fragments, and those with $\alpha > 0.6$ have two tenuous fragments. With non-zero β, the basic shape produced is a rotating disc with embedded higher density structures. Above and

below the disc is a bulge containing lower density material, the size of which increases with α. The line $\alpha = -\beta + 0.9$ roughly divides two regimes of the simulation. Above it, the simulations result in only an expanding and tenuous core where density increases only up to a factor of $\rho \approx 4$, containing either a single bar shaped fragment ($\beta < 0.4$) or two slightly separated elongated fragments ($\beta \geq 0.4$). On and below the line three higher density fragments embedded in a bar structure are produced, where one is at the centre of the core and two others located on the edges.

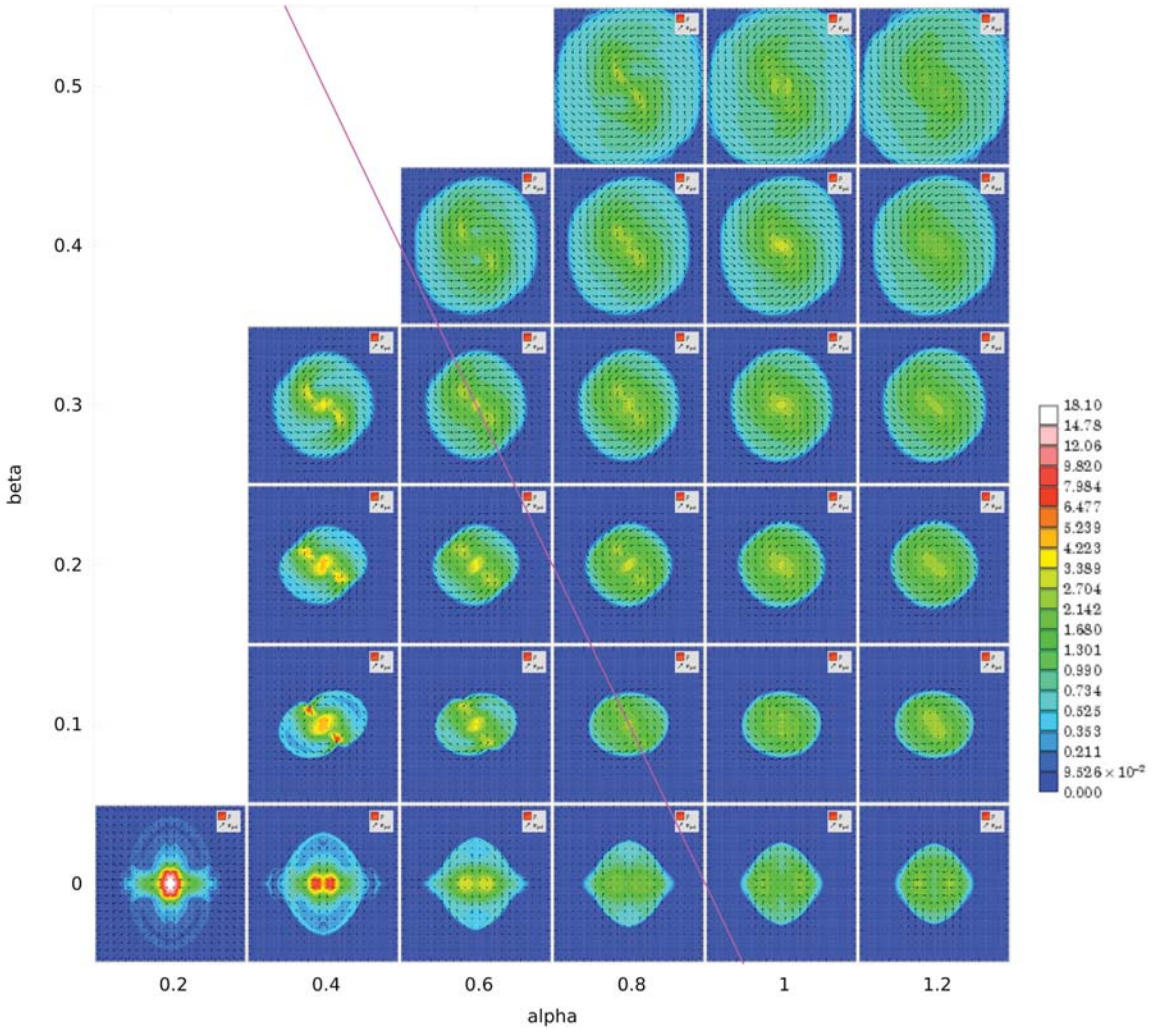

Figure 3.1: Equatorial slice of density at simulation end for $\zeta_m = 0.0$ (hydrodynamic) and $\gamma = 5/3$. The x and y axes are horizontal and vertical respectively. The line $\alpha = -\beta + 0.9$ is indicated.

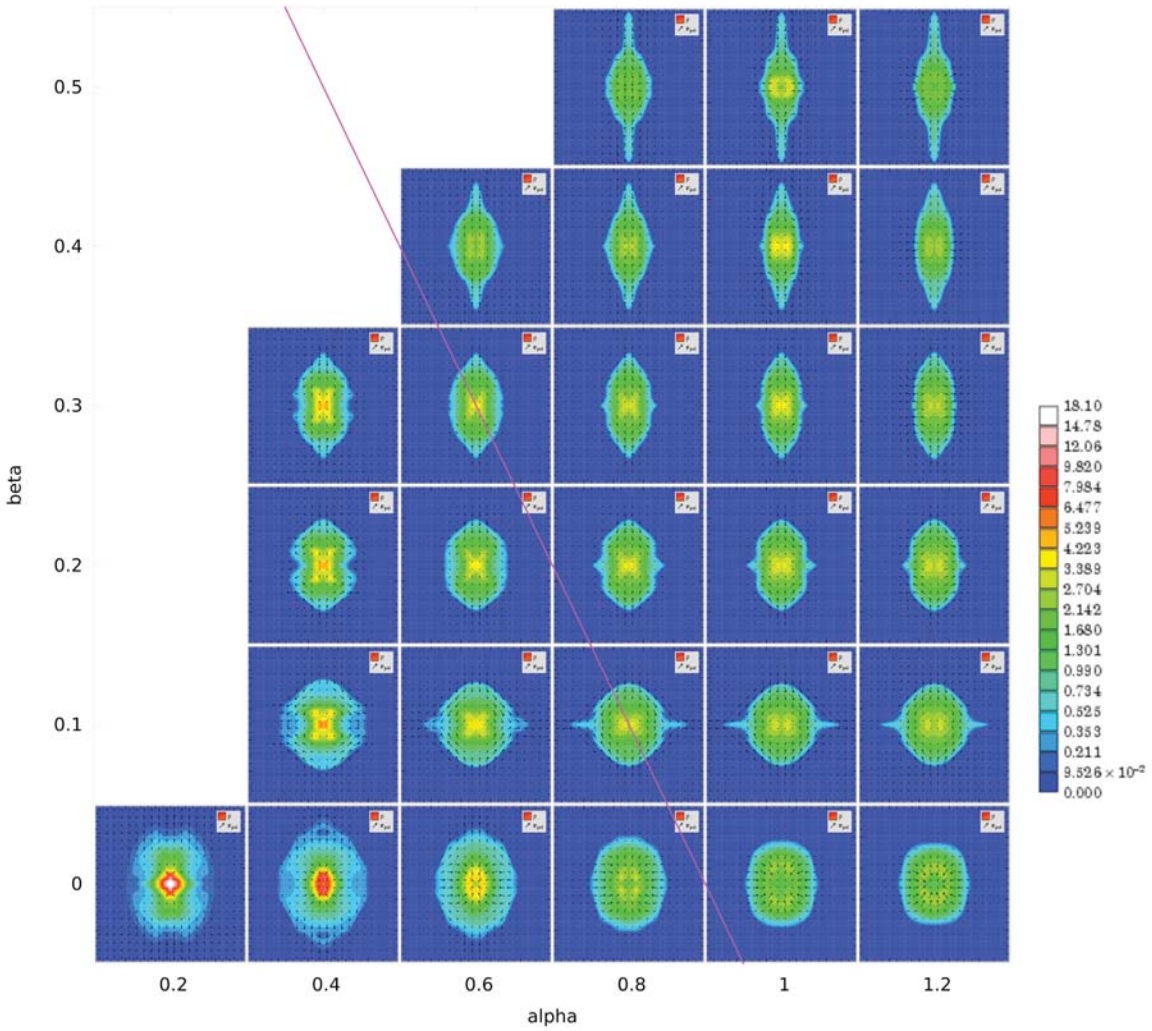

Figure 3.2: Rotation axis slice of density at simulation end $\zeta_m = 0.0$ (hydrodynamic) and $\gamma = 5/3$. The z and x axes are horizontal and vertical respectively. The line $\alpha = -\beta + 0.9$ is indicated.

The hydrodynamical simulation results for $\gamma = 4/3$ displayed in figures 3.3 and 3.4 are similar to the $\gamma = 5/3$ results, with the shape and maximum density of the collapsing core varying with changes to α and β in the same way. The $\beta = 0$ simulations have little difference with the corresponding $\gamma = 5/3$ cases, except that the dense regions are all close enough together to be considered one fragment. Once again, the line $\alpha = -\beta + 0.9$ roughly divides two regimes of rotating simulation

simulations. Above the line, the same expanding behaviour as the $\gamma = 5/3$ case occurs, and two low density fragments are produced when $\alpha \leq 1.0$. When $\alpha > 1.0$, a single central fragment is produced instead, the density of which increases with β. On and below the line, structures containing two higher density fragments connected by a bar of intermediate density emerge.

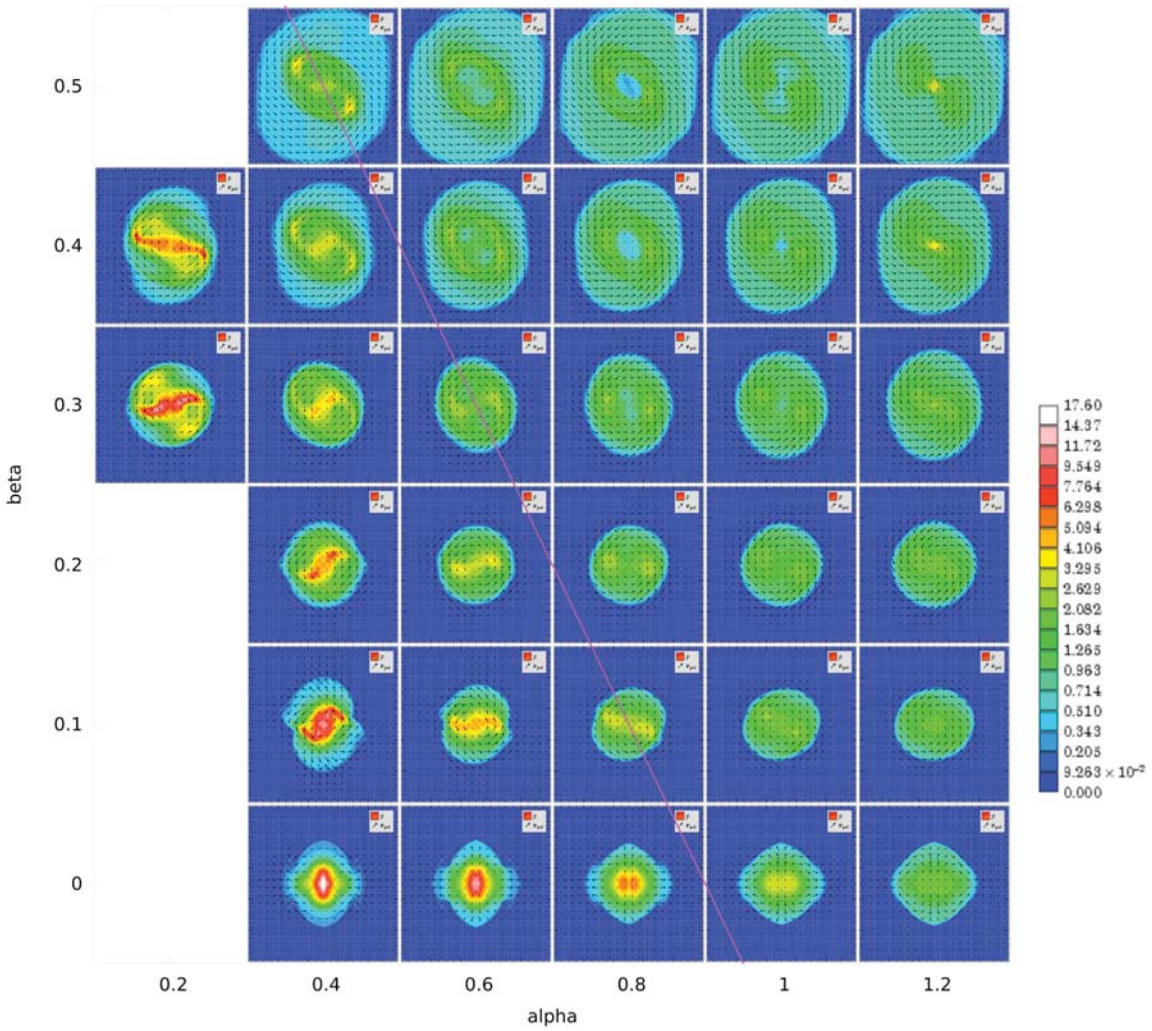

Figure 3.3: Equatorial slice of density at simulation end for $\zeta_m = 0.0$ and $\gamma = 4/3$.

For both sets of adiabatic hydrodynamical simulations, the maximum density is approximately constant across lines of slope $\dfrac{\alpha}{\beta} = 1$. This makes sense, since the

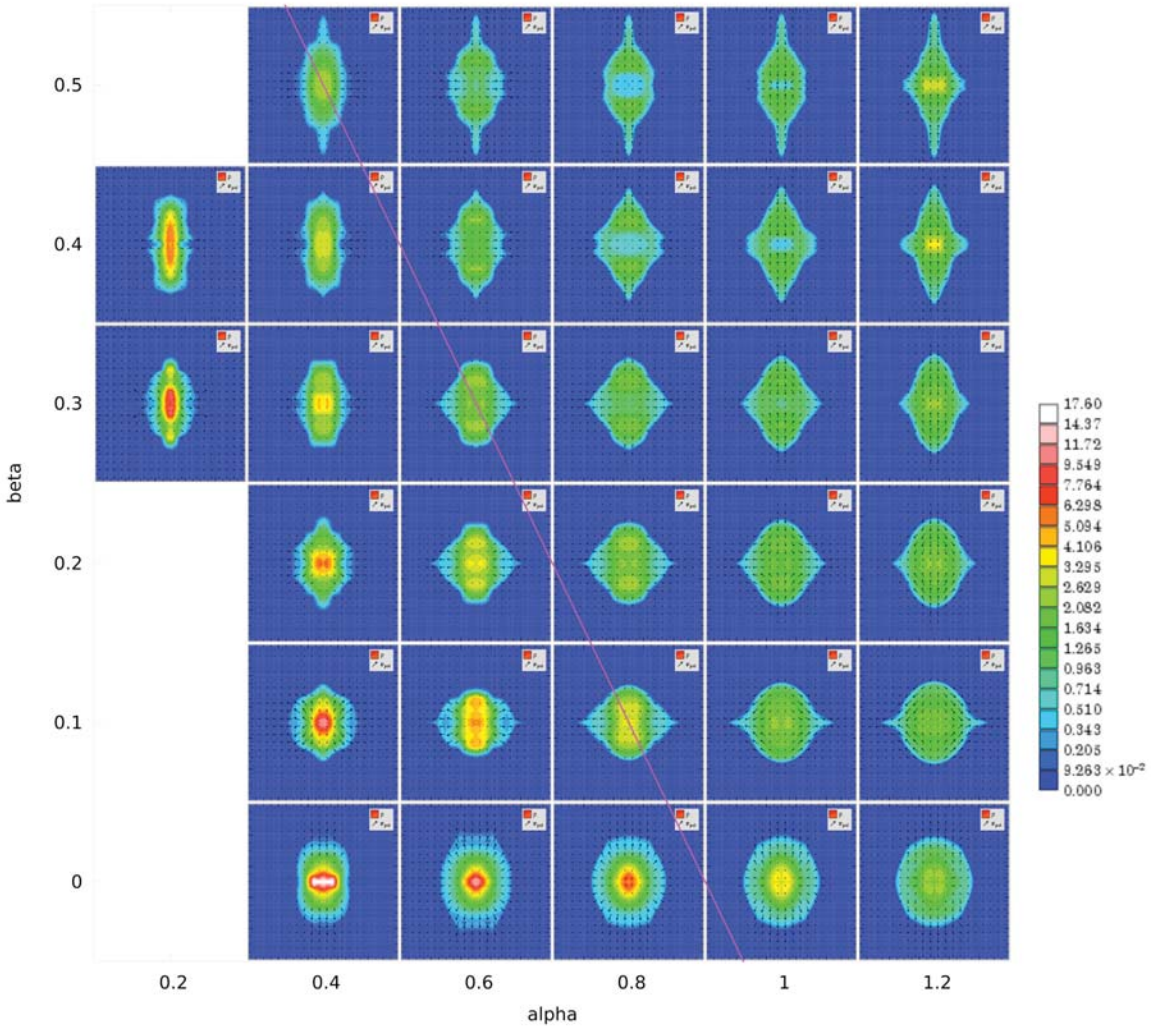

Figure 3.4: Rotation axis slice of density at simulation end $\zeta_m = 0.0$ and $\gamma = 4/3$.

resistance of the cloud to gravitational collapse increases with a larger supply of kinetic energy, and larger α and β both increase this either through thermal or rotational motion of the fluid.

The shape of the end state cores for the near-isothermal $\gamma = 1.001$ simulations differs greatly from the adiabatic simulations, but less conclusions can be drawn because over half of the simulations fail the Jeans condition. All of the available simulations collapse to form a disc or oblate sphere, flatter than in the adiabatic

cases. Curiously, simulations in the upper right corners of 3.5 and 3.6 with large α and β exhibit a low density 'hole' in the core, the opposite of what occurred in the $\gamma = 4/3$ case. The relationship between maximum density and β appears to be an increase in ρ up to a critical value of β, followed by a decrease beyond this point. However, this is not conclusive because of the lack of lower valued α and β Jeans compliant simulations. The simulations which evolve to the highest density are those

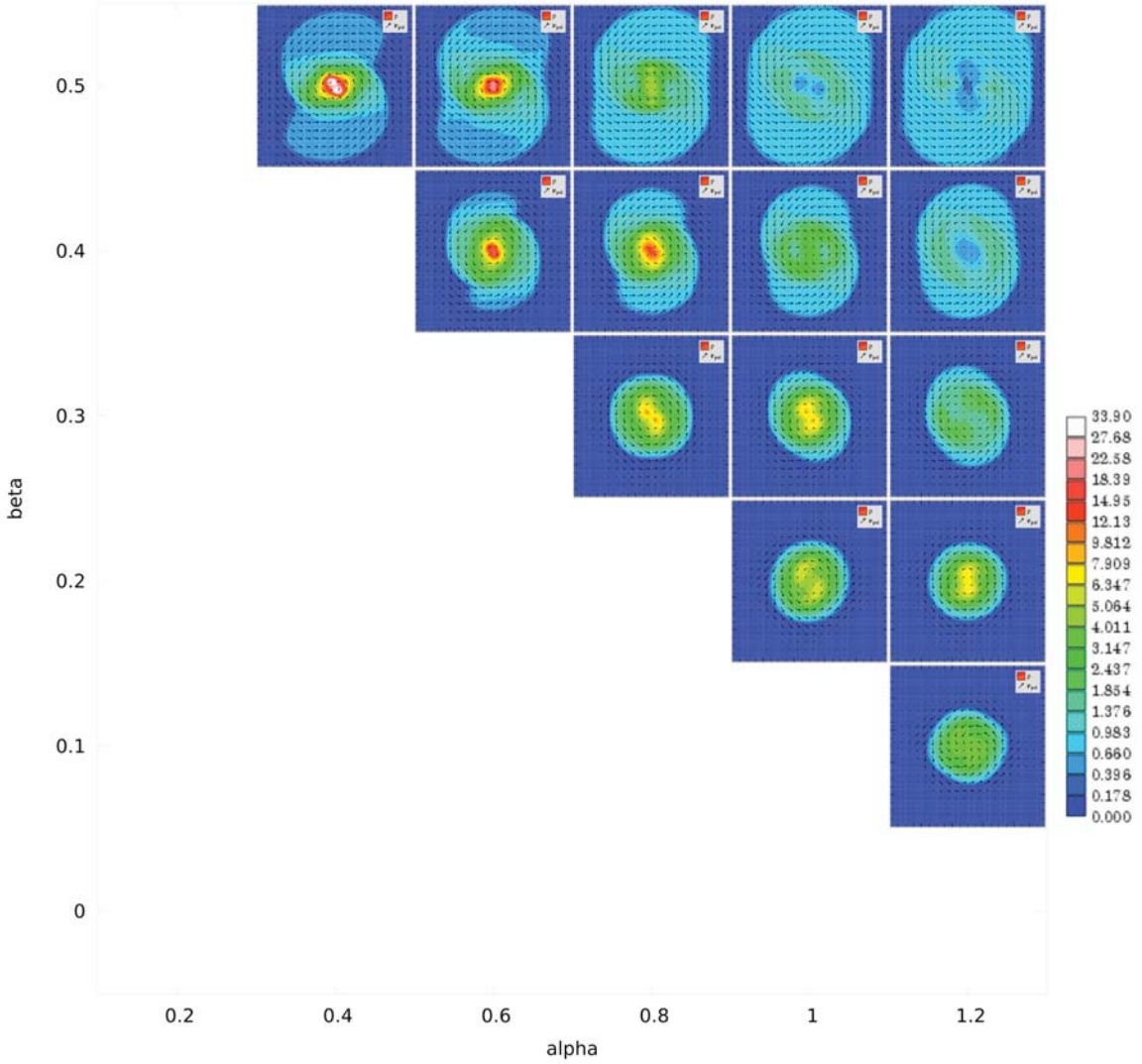

Figure 3.5: Equatorial slice of density at simulation end for $\zeta_m = 0.0$ and $\gamma = 1.001$.

with $\alpha = 0.4, 0.6$ and $\beta = 0.4, 0.5$, each containing only a single high density region.

Those with $\alpha = 0.8, 1.0$ and $\beta = 0.2, 0.3$ contain two regions of moderately high ($\rho \approx 7$) density, embedded in an S-shaped structure joining them. These regions are not considered fragments because lower isodensity surfaces enclose both of them, rather than each individually.

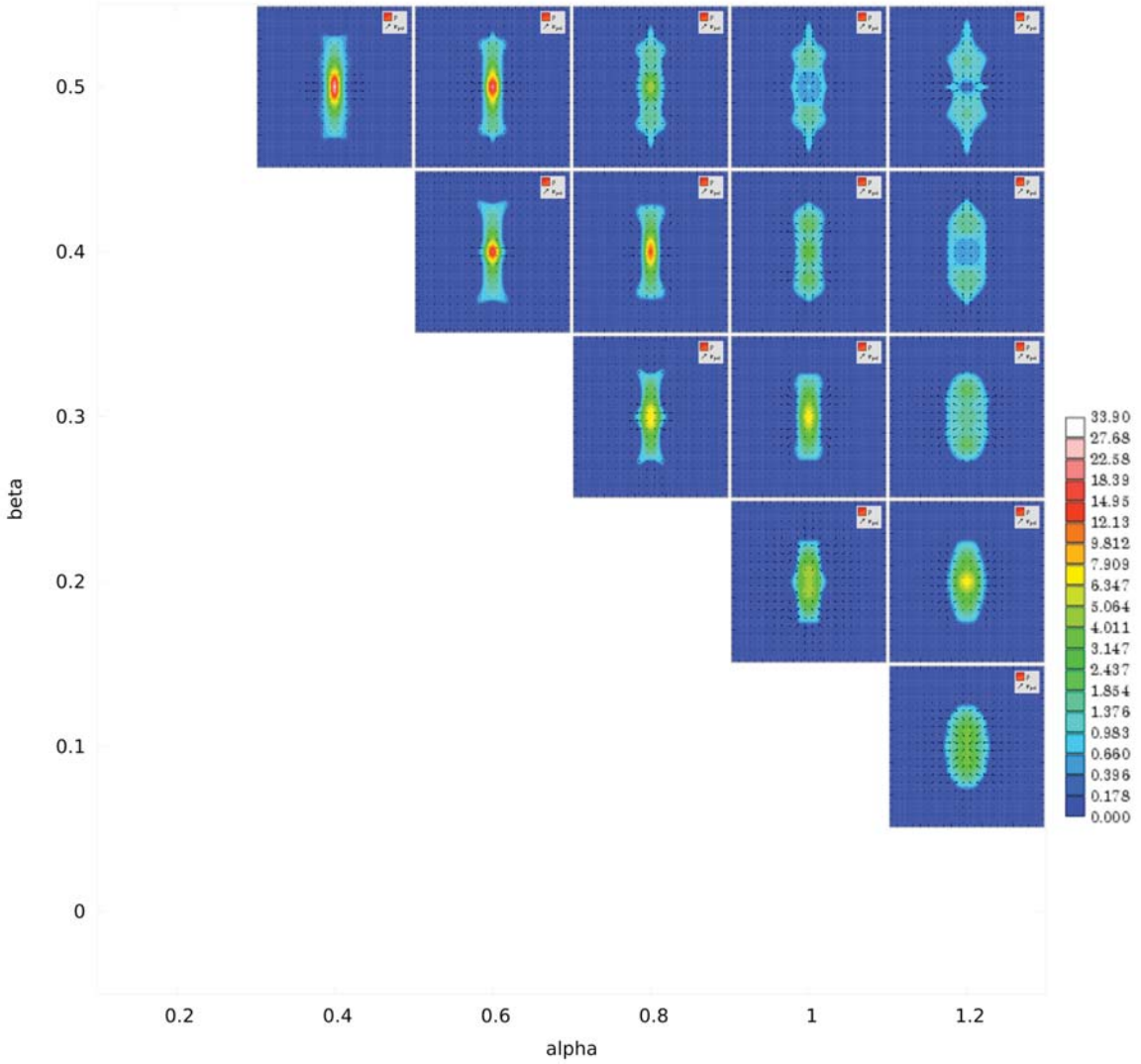

Figure 3.6: Rotation axis slice of density at simulation end $\zeta_m = 0.0$ and $\gamma = 1.001$.

Evidence of fragmentation is present for some of the hydrodynamical simulations, however, there are no high density regions of collapsed cores separated by a density contrast greater than ≈ 4. The best cases for fragmentation for each γ are those with

the parameters ($\alpha = 0.4, \beta = 0.2, \gamma = 4/3$),($\alpha = 0.4, \beta = 0.1, \gamma = 5/3$), and ($\alpha = 0.4, \beta = 0.5, \gamma = 1.001$). In general, any non-zero β simulations below the line $\alpha = -\beta + 0.9$ for the adiabatic simulations contain multiple fragments. Parameters which would cause the cloud to produce higher density fragments are likely in the regions of the parameter space which are Jeans condition non-compliant at this resolution, particularly those for the near-isothermal $\gamma = 1.001$ cases. These regions of the parameter space might be accessed with a higher resolution survey or the adaptive mesh refinement discussed in §1.3.2.

3.2 Magnetohydrodynamical Simulations

For the parameter space explored, simulations with the nonzero values of ζ_m used were observed to have quite similar end states. Hence, figures 3.7 to 3.12 display only one α–β parameter space slice for each value of γ. $\zeta_m = 0.5$ is shown for $\gamma = 5/3, 4/3$, while $\zeta_m = 2.0$ is shown for $\gamma = 1.001$, as these slices contain the most Jeans-condition compliant simulations.

The primary effect of the addition of a magnetic field aligned with the rotation axis is the containment of the fluid in rotating cores which would otherwise spread out perpendicular to the rotation axis. Increases to β result in fluid escaping from the core only along 4 tenuous arm structures, an example of which can be seen in the top row of figure 3.7. The number of arms is likely a result of the $m = 2$ perturbation mode used, although this has not been confirmed by testing with other perturbation modes. Adding magnetic fields provides so much support for the adiabatic cores that

the density increases by only up to a factor of 3.4 for $\gamma = 5/3$, and 5.3 for $\gamma = 4/3$. The result of further increasing ζ_m by a factor of two for any given MHD simulation is only a decrease in the maximum density of less than 10%, with any structure largely appearing the same.

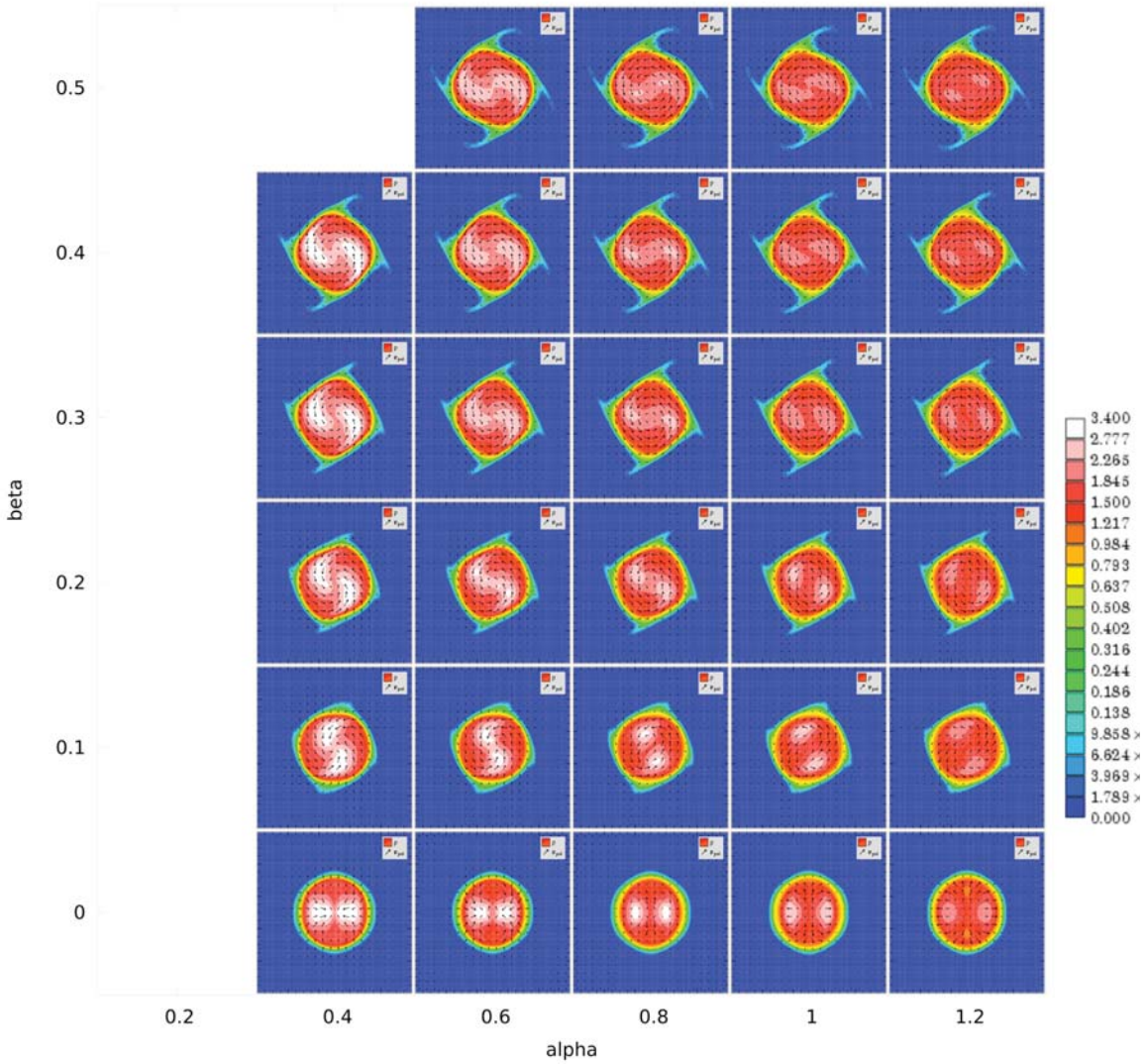

Figure 3.7: Equatorial slice of density at simulation end for $\zeta_m = 0.5$ and $\gamma = 5/3$. The magnetic field is parallel to the rotation axis, which points in the positive z direction.

Like the hydrodynamical simulations, the value of γ plays an important role in the shape of the end state of the core, with the adiabatic simulations exhibiting some

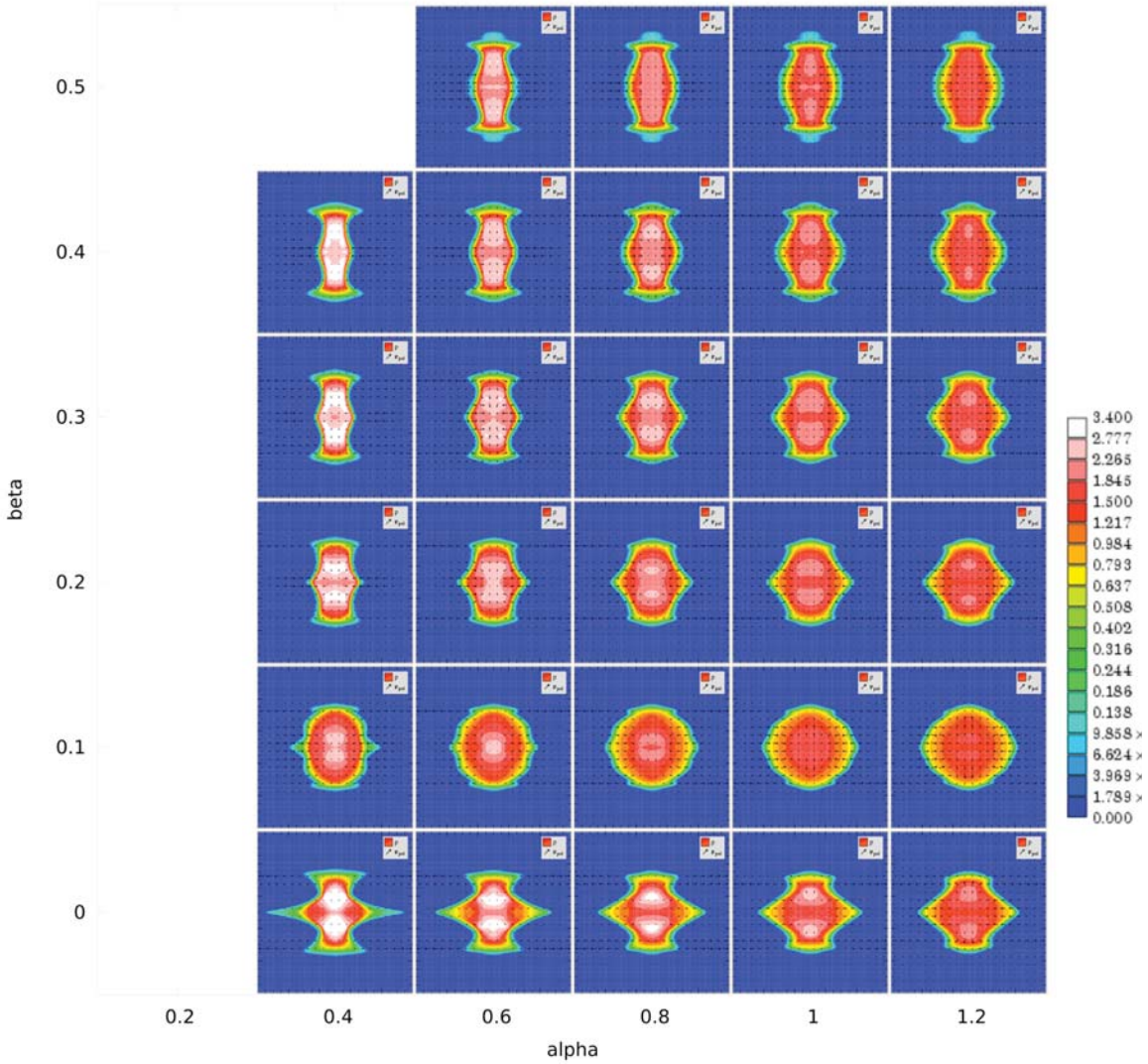

Figure 3.8: Rotation axis slice of density at simulation end for $\zeta_m = 0.5$ and $\gamma = 5/3$. The magnetic field is parallel to the rotation axis, which points in the positive z direction.

similarity. The $\gamma = 5/3$ simulations shown in figures 3.7 and 3.8 do not evolve to have much structure in the equatorial plane. Simulations with no rotation form two fragments which form closer together and increase in density with lower α. Simulations with rotation have only a low density ($\rho \sim 3$) S-shaped fragment containing two higher density regions for $\alpha < 0.8$. Values of α greater than this result in a nearly homogeneous core with two denser patches left from the original perturbation. The

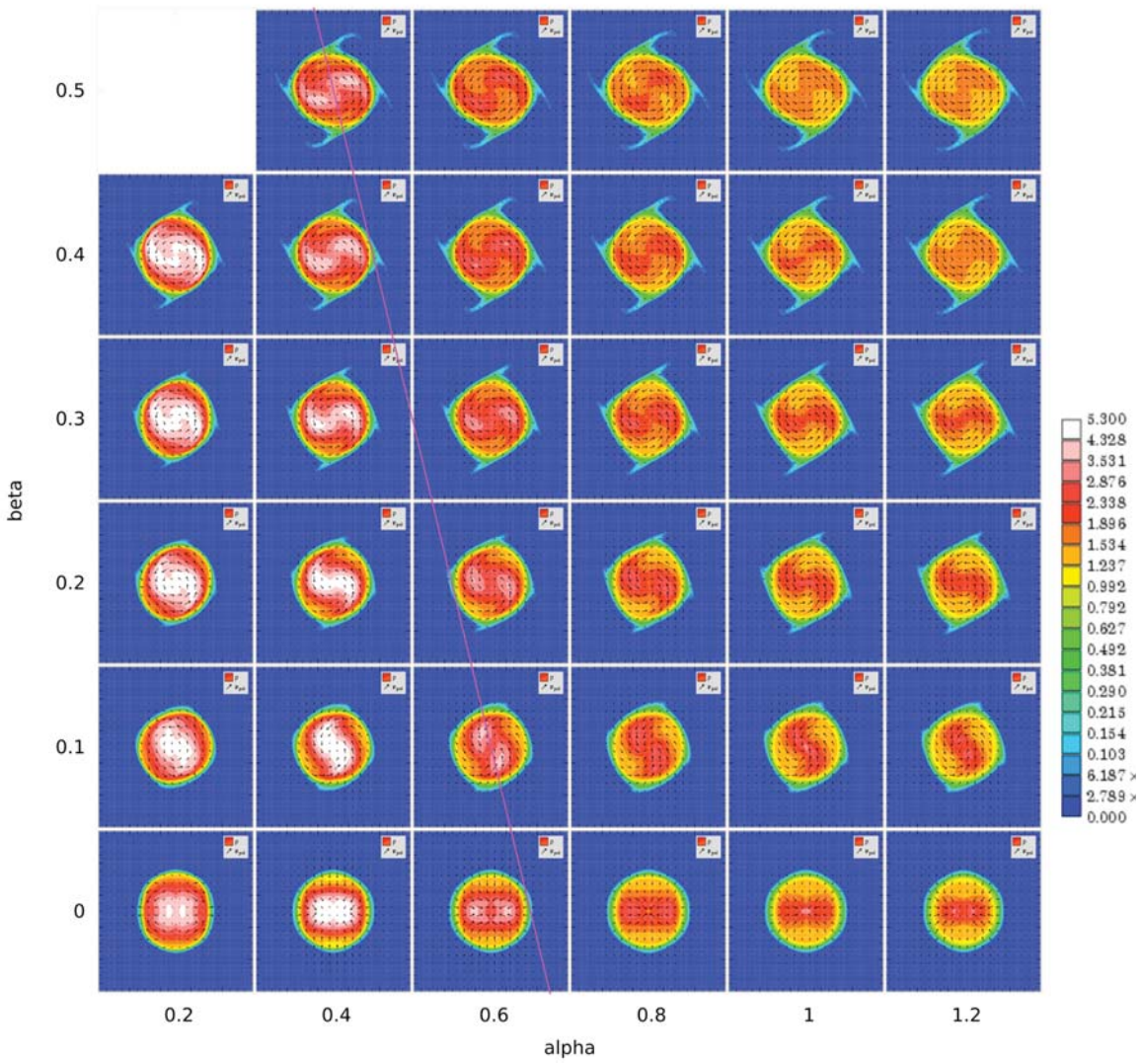

Figure 3.9: Equatorial slice of density at simulation end for $\zeta_m = 0.5$ and $\gamma = 4/3$. The line $\alpha = -\frac{1}{2}\beta + 0.65$ is indicated.

end state of the simulations along the rotation axis is shown in figure 3.8. For simulations without rotation, shown along the bottom row of figure 3.8, pointed bulges of low density material form along what would be the rotation axis, increasing in size for lower values of α. For non-zero β, the shape of the collapsed core is a lenticular disc containing the densest material, featuring low density "rims" of material extending downward and upward.

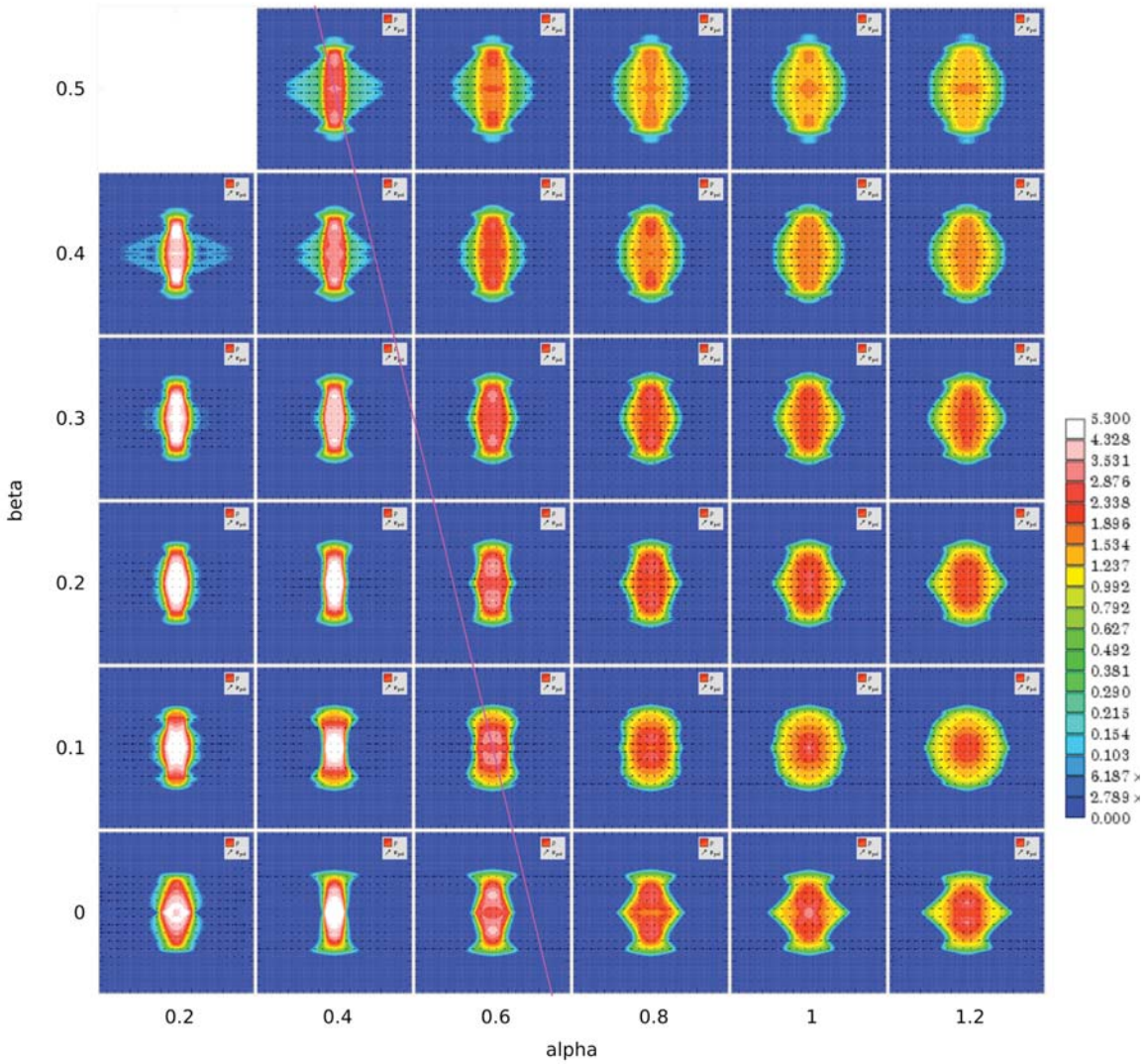

Figure 3.10: Rotation axis slice of density at simulation end for $\zeta_m = 0.5$ and $\gamma = 4/3$. The line $\alpha = -\frac{1}{2}\beta + 0.65$ is indicated.

For the $\gamma = 4/3$ group, simulations with $\beta = 0$ are similar in the equatorial plane to those with $\gamma = 5/3$, except that the two higher density regions form close enough together to be considered one fragment, the same relationship seen in the hydrodynamical adiabatic rotationless simulations. 3 different classes of shape emerge for rotating cores. Simulations on the line $\alpha = -\frac{1}{2}\beta + 0.65$ in figure 3.9 have denser regions in an S-shape containing two ($\rho \sim 4$) fragments and separated by a density

contrast of up to ~ 2. Simulations below this line produce an S-shaped bar containing

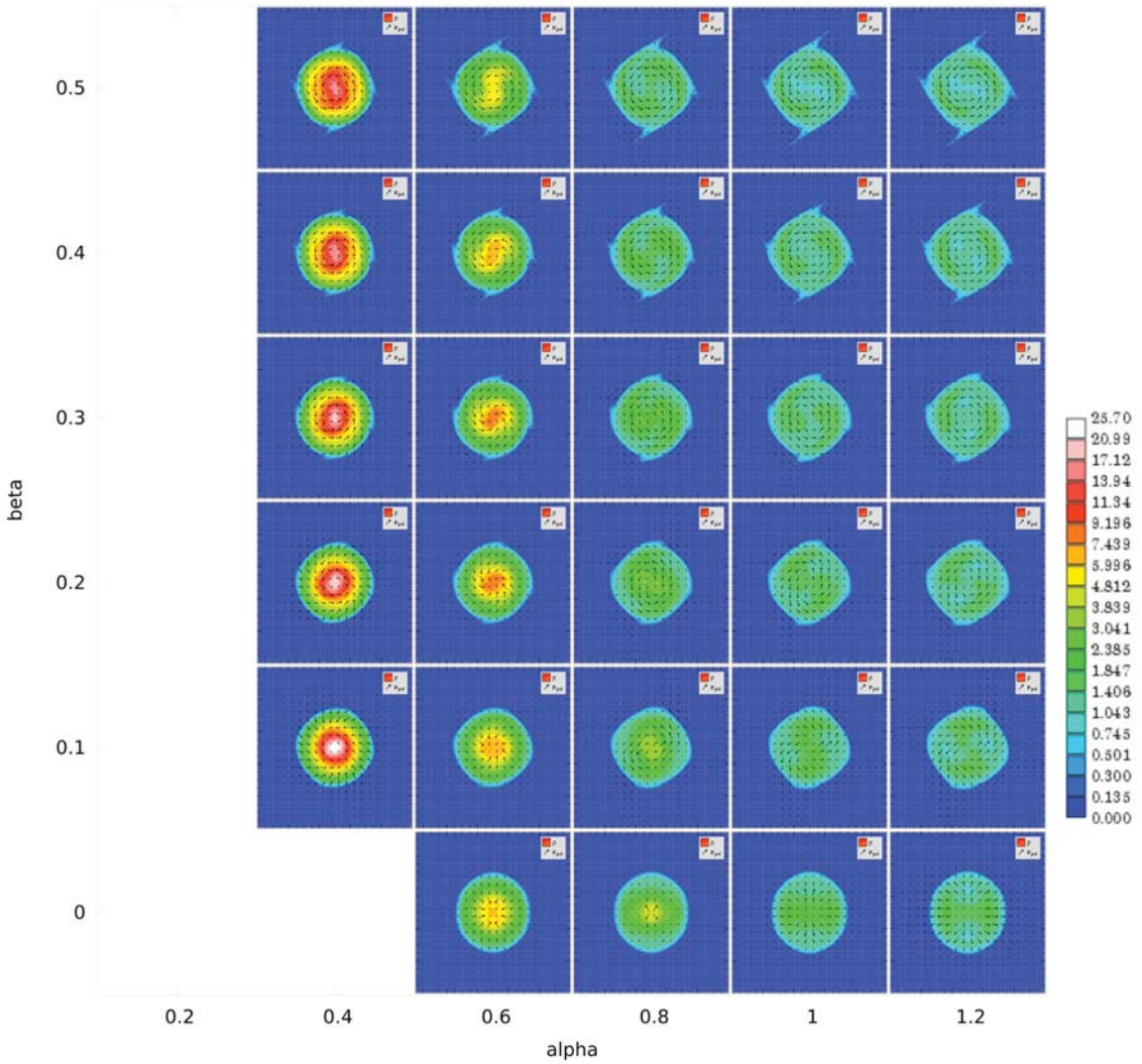

Figure 3.11: Equatorial slice of density at simulation end for $\zeta_m = 2.0$ and $\gamma = 1.001$.

one fragment, while those above have a shape reminiscent of the original perturbation, but distorted by rotation. In the plane of the rotation axis, the general shape of the core end state and behaviour with changes to α and β is similar to the $\gamma = 5/3$ case.

The near-isothermal MHD simulations displayed in figures 3.11 and 3.12 are much less affected by changes to β than other sets of simulations. Along columns of increasing β, simulations appear quite similar, apart from an elongation of the central

condensation and a smoothing out of the distribution of dense material. For simulations with $\alpha \leq 0.6$, a flattened disc is formed, while for those with $\alpha > 0.6$ a bulge of fluid away from the disc results, which increases in size with larger β.

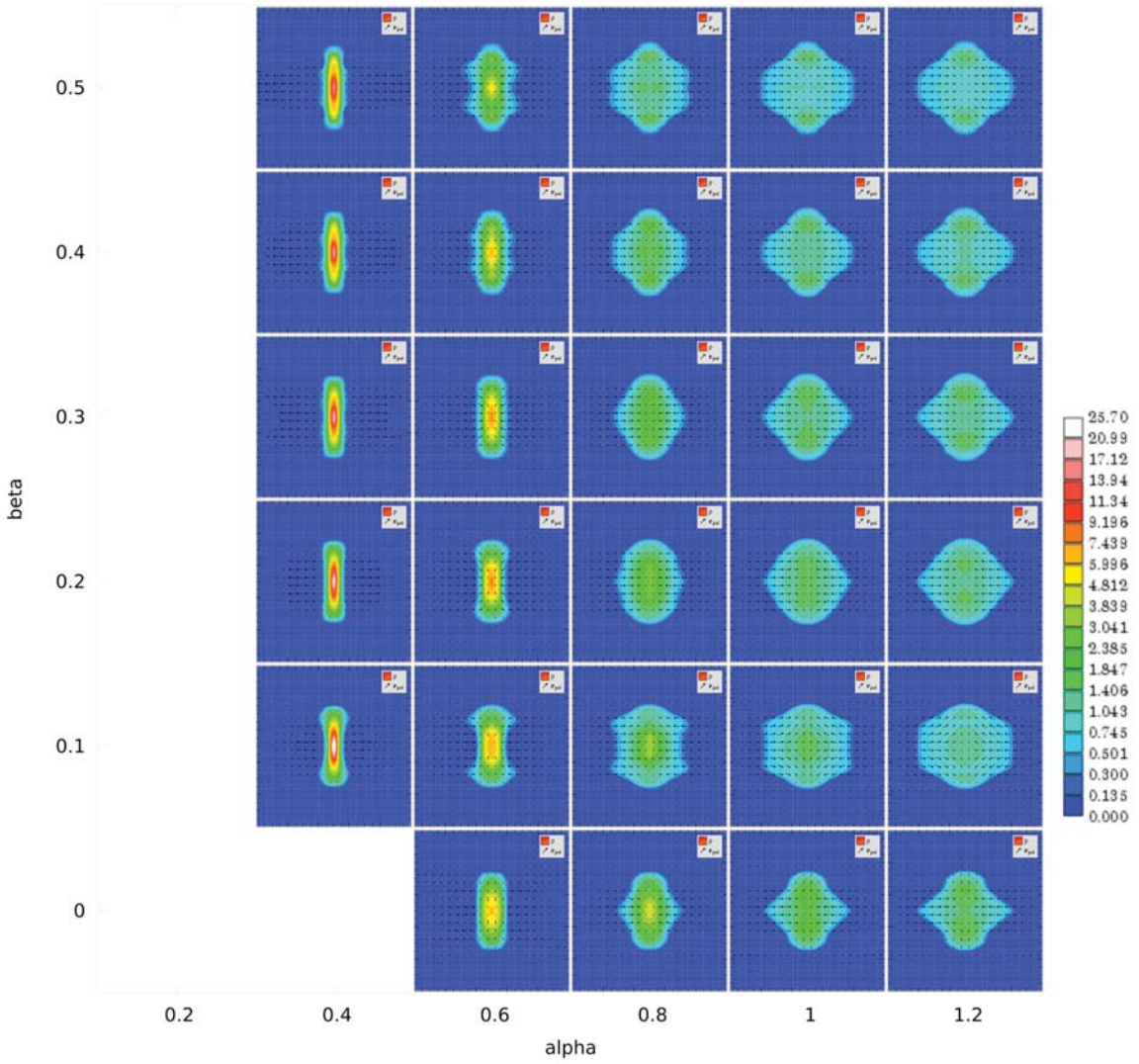

Figure 3.12: Rotation axis slice of density at simulation end for $\zeta_m = 2.0$ and $\gamma = 1.001$.

In general, significant support against collapse is provided by the magnetic fields, with all MHD simulations evolving to higher densities than their hydrodynamical counterparts and exhibiting more homogeneous structure. Less evidence of fragmen-

tation is also present in the MHD simulations, indicating that magnetic fields also tend to suppress fragmentation. The strongest cases for fragmentation for the adiabatic MHD simulations are $(\alpha = 0.8, \beta = 0.1, \zeta_m = 0.5, \gamma = 5/3)$ and $(\alpha = 0.6, \beta = 0.1, \zeta_m = 0.5, \gamma = 4/3)$, which both contain two fragments of maximum density $\rho \sim 3.4$ and $\rho \sim 5.3$ respectively. There are no MHD simulations for $\gamma = 1.001$ which convincingly form multiple fragments, but $(\alpha = 0.6, \beta = 0.5, \zeta_m = 2.0, \gamma = 1.001)$ comes closest with the formation of a single bar shaped fragment with a maximum density of $\rho \sim 6$.

Chapter 4

CONCLUSION

In the parameter space explored, the general effect of increasing the α, β, and ζ_m parameters was found to be the evolution of the perturbed spherical core to a state of lower density and larger size, demonstrating the support that increased thermal, rotational, and magnetic energy provides against gravitational collapse. The general shape of the collapsed core at simulation end was an oblate spheroid for $\beta = 0$ simulations, and a rotating disc sometimes exhibiting a bulge for $\beta \neq 0$ simulations. Increasing α results in a larger and lower density end state of the core, with the size increase reflected in either the radius of the oblate spheroid for $\beta = 0$ simulations, or the bulge and disc thickness for $\beta \neq 0$ simulations. Broadly, the effect of increasing β is an increase in radius of the disc and elongation of any fragments present. The addition of a rotation axis aligned magnetic field primarily homogenizes the density distribution of the collapsed core, contains fluid inside the disc (if present) and prevents expansion of the core perpendicular to field lines. Increasing β in simulations with a magnetic field results in the escape of a small amount of fluid along 4 trailing arm structures.

The effects of different values of γ are dramatic, and can be generalized into two cases: the adiabatic $\gamma = 5/3, 4/3$ and the near-isothermal $\gamma = 1.001$ simulations. The $\beta \neq 0$ $\gamma = 5/3$ hydrodynamical simulations are prone to producing 3 fragments for

simulations roughly on and below the line $\alpha = -\beta + 0.9$, and 2 fragments for the $\beta = 0$ hydrodynamical simulations. The $\gamma = 4/3$ hydrodynamical simulations behave in essentially the same way, but generally evolve to a higher density and produce two fragments on and below the $\alpha = -\beta + 0.9$ line, rather than three, and a single fragment for $\beta = 0$ simulations. The adiabatic hydrodynamical simulations evolve to approximately constant maximum densities across lines of $\frac{\alpha}{\beta} = 1$, indicating the equivalence of thermal and rotational energy in providing support against the collapse in this parameter space region. MHD simulations with $\gamma = 5/3$ evolve to homogenized and lower density states than their hydrodynamical counterparts, producing an S-shaped bar for $\beta \neq 0$ simulations with $\alpha < 0.8$ and two tenuous fragments for $\alpha/ge0.8$. MHD simulations with $\gamma = 4/3$ and $\beta \neq 0$ are more complicated, evolving to produce an S-shaped bar containging two fragments on the line $\alpha = -\frac{1}{2}\beta + 0.65$, a single bar shaped fragment for those below, and only a distortion of the original perturbation for those above. Near-isothermal simulations are quite different in character from the adiabtic simulations. In the hydrodynamical $\beta \neq 0$ case, the cores collapse to form a much thinner disc than in the adiabatic simulations, containing a single fragment for some simulations. A general trend could not be extracted because of the large number of simulations which failed the Jeans condition. the MHD near-isothermal simulations were much less prone to failing the Jeans condition, but produce only a single central condensation, indicating that fragmentation does not occur in this region of the parameter space. The addition of the field also nearly removes the dependence of the collapsed core morphology on β; simulations varying in β are nearly the same but for a slight elongation of the central condensation and smoothing of the

density distribution.

Although some conclusions were reached without the use of AMR, this technique would be incredibly useful for performing parameter space surveys for lower values of α and β, particularly in the near-isothermal hydrodynamical cases where the majority of the simulations failed the Jeans condition. Using AMR, the collapse of molecular cloud cores could be simulated in a physically realistic way to much higher densities, allowing further examination of process of multiple star system formation.

Appendix A

Derivation of the Magnetic Critical Mass

Following the derivation by Krumholz (2011), the magnetic critical mass for a uniform sphere penetrated by a uniform magnetic field is derived using the virial theorem modified to include magnetic energy (1.11), with the kinetic energy contribution assumed to be negligible:

$$\langle E_{\text{mag.}} \rangle + \langle U \rangle = 0. \tag{A.1}$$

Substituting $E_{\text{mag.}}$ (1.12) and U with equation (1.3) and solving for the critical magnetic mass M_B:

$$-\frac{3GM_B^2}{5R} + \frac{2\Phi_B^2}{\mu_0 \pi R} = 0 \tag{A.2}$$

$$M_B^2 = \left(\frac{2\Phi_B^2}{\mu_0 \pi R}\right)\left(\frac{5}{3G}\right) \tag{A.3}$$

$$M_B = \left(\frac{10\Phi_B^2}{3\mu_0 \pi}\right)^{1/2} \tag{A.4}$$

Appendix B

Solving Poisson's equation in 3 Cartesian Dimensions

The following ways of solving Poisson's equation in *ZEUS-3D* are based on a methods detailed by Press et al. (1992).

Using the Laplacian in Cartesian coordinates, Poisson's equation is written as:

$$\frac{\partial^2\phi}{\partial x^2} + \frac{\partial^2\phi}{\partial y^2} + \frac{\partial^2\phi}{\partial z^2} = \rho(x, y, z). \tag{B.1}$$

Replacing the second partial derivatives with 2nd order centred differences:

$$\begin{aligned} &\frac{\phi_{j+1,k,l} - 2\phi_{j,k,l} + \phi_{j-1,k,l}}{\Delta_x^2} + \frac{\phi_{j,k+1,l} - 2\phi_{j,k,l} + \phi_{j,k-1,l}}{\Delta_y^2} + \\ &\frac{\phi_{j,k,l+1} - 2\phi_{j,k,l} + \phi_{j,k,l-1}}{\Delta_z^2} = \rho_{j,k,l}, \end{aligned} \tag{B.2}$$

where

$\Delta_x, \Delta_y, \Delta_z,$	are the dimensions of a zone;
$j = 0, 1, \ldots, J$	$x_j = x_0 + j\Delta_x;$
$k = 0, 1, \ldots, K$	$y_k = y_0 + k\Delta_y;$
$l = 0, 1, \ldots, L$	$z_l = z_0 + l\Delta_z;$
$\phi(x_j, y_k, z_l) \equiv \phi_{j,k,l};$	

$$\rho(x_j, y_k, z_l) \equiv \rho_{j,k,l}.$$

For convenience, multiply (B.2) by $(\Delta_x \Delta_y \Delta_z)^2$ to arrive at:

$$\begin{aligned}&(\Delta_y \Delta_z)^2(\phi_{j+1,k,l} - 2\phi_{j,k,l} + \phi_{j-1,k,l}) + (\Delta_x \Delta_z)^2(\phi_{j,k+1,l} - 2\phi_{j,k,l} + \phi_{j,k-1,l}) + \\ &(\Delta_x \Delta_y)^2(\phi_{j,k,l+1} - 2\phi_{j,k,l} + \phi_{j,k,l-1}) = (\Delta_x \Delta_y \Delta_z)^2 \rho_{j,k,l}.\end{aligned} \tag{B.3}$$

B.1 Zero and Inhomogeneous Boundary Conditions

For all simulations in this thesis, inhomogeneous boundary conditions are used. In 3 Cartesian dimensions, the inverse (i.e., including normalization) DST for some discretized function f is:

$$\begin{aligned}f_{j,k,l} &= \frac{8}{JKL} \sum_{m=1}^{J-1} \sum_{n=1}^{K-1} \sum_{o=1}^{L-1} \hat{f}_{m,n,o} S_{j,k,l,m,n,o}, \\ S_{j,k,l,m,n,o} &\equiv \sin\left(\frac{\pi j m}{J}\right) \sin\left(\frac{\pi k n}{K}\right) \sin\left(\frac{\pi l o}{L}\right).\end{aligned} \tag{B.4}$$

Substituting the DST for $\phi_{j,k,l}$ and $\rho_{j,k,l}$ into (B.3) and dividing out the normalization:

$$\begin{aligned}
&(\Delta_y\Delta_z)^2\sum_{m=1}^{J-1}\sum_{n=1}^{K-1}\sum_{o=1}^{L-1}\phi_{m,n,o}(S_{j+1,k,l,m,n,o}-2S_{j,k,l,m,n,o}+S_{j-1,k,l,m,n,o})+\\
&(\Delta_x\Delta_z)^2\sum_{m=1}^{J-1}\sum_{n=1}^{K-1}\sum_{o=1}^{L-1}\phi_{m,n,o}(S_{j,k+1,l,m,n,o}-2S_{j,k,l,m,n,o}+S_{j,k-1,l,m,n,o})+\\
&(\Delta_x\Delta_y)^2\sum_{m=1}^{J-1}\sum_{n=1}^{K-1}\sum_{o=1}^{L-1}\phi_{m,n,o}(S_{j,k,l+1,m,n,o}-2S_{j,k,l,m,n,o}+S_{j,k,l-1,m,n,o})\ =\\
&(\Delta_x\Delta_y\Delta_z)^2\sum_{m=1}^{J-1}\sum_{n=1}^{K-1}\sum_{o=1}^{L-1}\hat{\rho}_{m,n,o}S_{j,k,l,m,n,o}.
\end{aligned} \tag{B.5}$$

By virtue of the linear independence of the functions in the sums in (B.5) , a similar expression which holds for any m, n, or o can be created:

$$\begin{aligned}
\hat{\phi}_{m,n,o}\Bigg\{&(\Delta_y\Delta_z)^2\sin\left(\frac{\pi kn}{K}\right)\sin\left(\frac{\pi lo}{L}\right)\left[\sin\left(\frac{\pi(j+1)m}{J}\right)-2\sin\left(\frac{\pi jm}{J}\right)+\right.\\
&\left.\sin\left(\frac{\pi(j-1)m}{J}\right)\right]+\\
&(\Delta_x\Delta_z)^2\sin\left(\frac{\pi jm}{J}\right)\sin\left(\frac{\pi lo}{L}\right)\left[\sin\left(\frac{\pi(k+1)n}{K}\right)-2\sin\left(\frac{\pi kn}{K}\right)+\right.\\
&\left.\sin\left(\frac{\pi(k-1)n}{K}\right)\right]+\\
&(\Delta_x\Delta_y)^2\sin\left(\frac{\pi jm}{J}\right)\sin\left(\frac{\pi kn}{K}\right)\left[\sin\left(\frac{\pi(l+1)o}{L}\right)-2\sin\left(\frac{\pi lo}{L}\right)+\right.\\
&\left.\sin\left(\frac{\pi(l-1)o}{L}\right)\right]\Bigg\}=\\
&(\Delta_x\Delta_y\Delta_z)^2\sin\left(\frac{\pi jm}{J}\right)\sin\left(\frac{\pi kn}{K}\right)\sin\left(\frac{\pi lo}{L}\right)\hat{\rho}_{m,n,o},
\end{aligned} \tag{B.6}$$

where common terms in $S_{j,k,l,m,n,o}$ have been factored out. The terms in square brackets can be further simplified with the identity $\sin(A+B)=\sin(A)\cos(B)+$

$\cos(A)\sin(B)$, e.g.:

$$\begin{aligned}
&\sin\left(\frac{\pi(j+1)m}{J}\right) - 2\sin\left(\frac{\pi jm}{J}\right) + \sin\left(\frac{\pi(j-1)m}{J}\right) = \\
&\sin\left(\frac{\pi jm}{J}\right)\cos\left(\frac{\pi m}{J}\right) + \cos\left(\frac{\pi jm}{J}\right)\sin\left(\frac{\pi m}{J}\right) - 2\sin\left(\frac{\pi jm}{J}\right) + \\
&\sin\left(\frac{\pi jm}{J}\right)\cos\left(-\frac{\pi m}{J}\right) + \cos\left(\frac{\pi jm}{J}\right)\sin\left(-\frac{\pi m}{J}\right) = \\
&2\sin\left(\frac{\pi jm}{J}\right)\cos\left(\frac{\pi m}{J}\right) - 2\sin\left(\frac{\pi jm}{J}\right) = \\
&2\sin\left(\frac{\pi jm}{J}\right)\left(\cos\left(\frac{\pi m}{J}\right) - 1\right).
\end{aligned} \tag{B.7}$$

Performing the simplification in (B.7) for all terms in square brackets and then dividing out the $\sin\left(\frac{\pi jm}{J}\right)\sin\left(\frac{\pi kn}{K}\right)\sin\left(\frac{\pi lo}{L}\right)$ factor leads to:

$$\begin{aligned}
\hat{\phi}_{m,n,o}\Bigg\{2(\Delta_y\Delta_z)^2\left[\left(\cos\left(\frac{\pi m}{J}\right) - 1\right)\right] + 2(\Delta_x\Delta_z)^2\left[\left(\cos\left(\frac{\pi n}{K}\right) - 1\right)\right] + \\
2(\Delta_x\Delta_y)^2\left[\left(\cos\left(\frac{\pi o}{L}\right) - 1\right)\right]+\Bigg\} = (\Delta_x\Delta_y\Delta_z)^2\hat{\rho}_{m,n,o},
\end{aligned} \tag{B.8}$$

which can be solved for $\hat{\phi}_{m,n,o}$ to arrive at the algebra used to calculate the potential in Fourier space:

$$\begin{aligned}
\hat{\phi}_{m,n,o} = (\Delta_x\Delta_y\Delta_z)^2\hat{\rho}_{m,n,o}\Bigg\{2(\Delta_y\Delta_z)^2\left[\left(\cos\left(\frac{\pi m}{J}\right) - 1\right)\right] + \\
2(\Delta_x\Delta_z)^2\left[\left(\cos\left(\frac{\pi n}{K}\right) - 1\right)\right] + 2(\Delta_x\Delta_y)^2\left[\left(\cos\left(\frac{\pi o}{L}\right) - 1\right)\right]+\Bigg\}^{-1}.
\end{aligned} \tag{B.9}$$

The Poisson's equation solver implemented in *ZEUS-3D* uses repeated application

of a 1-D FST routine by Press et al. (1992) to compute $\hat{\rho}$ with:

$$\hat{f}_{m,n,o} = \frac{8}{JKL} \sum_{j=1}^{J-1} \sum_{k=1}^{K-1} \sum_{l=1}^{L-1} f_{j,k,l} S_{j,k,l,m,n,o}, \tag{B.10}$$

then solves for $\hat{\phi}$ using (B.9), and then computes ϕ using (B.4) for every non-boundary point on the grid. This procedure is valid for zero boundary conditions for ϕ. If inhomogeneous boundaries are desired, ρ can be modified to incorporate them. Consider (B.3) evaluated at $j = J - 1$:

$$(\Delta_y \Delta_z)^2(\phi_{J,k,l} - 2\phi_{J-1,k,l} + \phi_{J-2,k,l}) + (\Delta_x \Delta_z)^2(\phi_{J-1,k+1,l} - 2\phi_{J-1,k,l} + \phi_{J-1,k-1,l}) +$$
$$(\Delta_x \Delta_y)^2(\phi_{J-1,k,l+1} - 2\phi_{J-1,k,l} + \phi_{J-1,k,l-1}) = (\Delta_x \Delta_y \Delta_z)^2 \rho_{J-1,k,l}. \tag{B.11}$$

If the $\phi_{J,k,l}$ boundary term containing the boundary conditions at the J face of the grid (which would otherwise be zero) is brought over to the right hand side, solving (B.11) is identical to the case of zero boundary conditions, but for a density distribution modified by the subtraction of the $\phi_{J,k,l}$ boundary from the $J-1$ slice of $\rho_{j,k,l}$. Thus, to include an inhomogeneous J boundary, the replacement:

$$\rho_{J-1,k,l} \rightarrow \rho_{J-1,k,l} - \frac{\phi_{J,k,l}}{\Delta_x^2}, \tag{B.12}$$

is used. Analogous modifications are made for the 5 other boundary faces of the grid.

B.2 Periodic Boundary Conditions

Although not used in this thesis, the routines developed in *ZEUS-3D* are also capable of solving Poisson's equation with periodic boundary conditions, which are a common choice for astrophysical simulations. In 3 Cartesian dimensions, the DFT and its inverse are respectively:

$$\hat{f}_{m,n,o} = \sum_{j=0}^{J-1}\sum_{k=0}^{K-1}\sum_{l=0}^{L-1} f_{j,k,l} e^{2\pi ijm/J} e^{2\pi ikn/K} e^{2\pi ilo/L}, \tag{B.13}$$

$$f_{j,k,l} = \frac{1}{JKL}\sum_{m=0}^{J-1}\sum_{n=0}^{K-1}\sum_{o=0}^{L-1} \hat{f}_{m,n,o} e^{-2\pi ijm/J} e^{-2\pi ikn/K} e^{-2\pi ilo/L}. \tag{B.14}$$

When equation (B.14) is substituted into (B.3) and manipulated in a manner similar to the DST case, the Fourier space algebra used for calculating the potential with periodic boundary conditions can be found:

$$\hat{\phi}_{m,n,o} = (\Delta_x\Delta_y\Delta_z)^2 \hat{\rho}_{m,n,o} \Bigg\{ 2(\Delta_y\Delta_z)^2 \left[\left(\cos\left(\frac{2\pi m}{J}\right) - 1 \right) \right] + 2(\Delta_x\Delta_z)^2 \left[\left(\cos\left(\frac{2\pi n}{K}\right) - 1 \right) \right] + 2(\Delta_x\Delta_y)^2 \left[\left(\cos\left(\frac{2\pi o}{L}\right) - 1 \right) \right] + \Bigg\}^{-1}. \tag{B.15}$$

It should be noted that a divergent point appears for $m = n = o = 0$, which is set to zero in *ZEUS-3D*. Other than this, the process for computing $\hat{\phi}$ is then the same as the zero boundary condition case, but with equations (B.10), (B.9), and (B.4) replaced by equations (B.13), (B.15), and (B.14) respectively.

Bibliography

M. J. Berger and P. Colella. Local adaptive mesh refinement for shock hydrodynamics. *Journal of Computational Physics*, 82:64–84, May 1989.

M. J. Berger and J. Oliger. Adaptive Mesh Refinement for Hyperbolic Partial Differential Equations. *Journal of Computational Physics*, 53:484–512, March 1984.

A. P. Boss. Collapse and fragmentation of molecular cloud cores. I - Moderately centrally condensed cores. *Astrophysical Journal*, 410:157–167, June 1993.

A. Burkert and P. Bodenheimer. Multiple Fragmentation in Collapsing Protostars. *Monthly Notices of the RAS*, 264:798, October 1993.

B. W. Carroll and D. A. Ostlie. *An Introduction to Modern Astrophysics*. Addison-Wesley, 1301 Sansome St., San Francisco, CA 94111, second edition, 2007.

D. A. Clarke. A Consistent Method of Characteristics for Multidimensional Magnetohydrodynamics. *Astrophysical Journal*, 457:291, January 1996.

D. A. Clarke. On the Reliability of ZEUS-3D. *Astrophysical Journal, Supplement*, 187:119–134, March 2010.

D. A. Clarke, N. R. Macdonald, J. P. Ramsey, and M. Richardson. Astrophysical Jets. *Physics in Canada*, 64:47–53, April 2008.

J. Cooley and J. Tukey. An algorithm for the machine calculation of complex fourier series. *Mathematics of Computation*, 19(90):297–301, 1965.

G. C. Danielson and C. Lanczos. Some improvements in practical fourier analysis and their application to x-ray scattering from liquids. *Journal of The Franklin Institute*, 233:365–380 and 435–452, 1942.

A. Duquennoy and M. Mayor. Multiplicity among solar-type stars in the solar neighbourhood. II - Distribution of the orbital elements in an unbiased sample. *Astronomy and Astrophysics*, 248:485–524, August 1991.

B. G. Elmegreen. The formation of giant cloud complexes by the Parker-Jeans instability. *Astrophysical Journal*, 253:655–665, February 1982.

K. M. Ferrière. The interstellar environment of our galaxy. *Reviews of Modern Physics*, 73:1031–1066, October 2001.

M. R. Krumholz. Star Formation in Molecular Clouds. In E. Telles, R. Dupke, and D. Lazzaro, editors, *American Institute of Physics Conference Series*, volume 1386 of *American Institute of Physics Conference Series*, pages 9–57, September 2011.

J. Kwan and F. Valdes. Spiral gravitational potentials and the mass growth of molecular clouds. *Astrophysical Journal*, 271:604–610, August 1983.

C. J. Lada. Stellar Multiplicity and the Initial Mass Function: Most Stars Are Single. *Astrophysical Journal, Letters*, 640:L63–L66, March 2006.

R. Launhardt, A. I. Sargent, T. Henning, R. Zylka, and H. Zinnecker. Binary and multiple star formation in Bok globules. In *IAU Symposium*, volume 200 of *IAU Symposium*, page 103P, 2000.

C. F. McKee and E. C. Ostriker. Theory of Star Formation. *Annual Review of Astronomy and Astrophysics*, 45:565–687, September 2007.

C. F. McKee and J. P. Ostriker. A theory of the interstellar medium - Three components regulated by supernova explosions in an inhomogeneous substrate. *Astrophysical Journal*, 218:148–169, November 1977.

S. McMillan. Jeans instability and gravitational collapse. `http://www.physics.drexel.edu/students/courses/physics-502/jeans_instability.pdf`, January 2014.

S. Narita, C. Hayashi, and S. M. Miyama. Characteristics of Collapse of Rotating Isothermal Clouds. *Progress of Theoretical Physics*, 72:1118–1136, December 1984.

M. L. Norman, J. R. Wilson, and R. T. Barton. A new calculation on rotating protostar collapse. *Astrophysical Journal*, 239:968–981, August 1980.

W. H. Press, B. P. Flannery, S. A. Teukolsky, and W. T. Vetterling. *Numerical Recipes in FORTRAN 77: The Art of Scientific Computing*. Cambridge University Press, 2 edition, September 1992.

D. Prialnik. *An Introduction to the Theory of Stellar Structure and Evolution*. Cambridge University Press, 32 Avenue of the Americas, New York, NY 10013-2473, USA, first edition, 2000.

R. E. Pudritz. Clustered Star Formation. In T. Montmerle and P. André, editors, *From Darkness to Light: Origin and Evolution of Young Stellar Clusters*, volume 243 of *Astronomical Society of the Pacific Conference Series*, page 3, 2001.

J. P. Ramsey, D. A. Clarke, and A. B. Men'shchikov. AZEuS: An Adaptive Zone Eulerian Scheme for Computational Magnetohydrodynamics. *Astrophysical Journal, Supplement*, 199:13, March 2012.

J. K. Truelove, R. I. Klein, C. F. McKee, J. H. Holliman, II, L. H. Howell, and J. A. Greenough. The Jeans Condition: A New Constraint on Spatial Resolution in Simulations of Isothermal Self-gravitational Hydrodynamics. *Astrophysical Journal, Letters*, 489:L179, November 1997.

J. K. Truelove, R. I. Klein, C. F. McKee, J. H. Holliman, II, L. H. Howell, J. A. Greenough, and D. T. Woods. Self-gravitational Hydrodynamics with Three-dimensional Adaptive Mesh Refinement: Methodology and Applications to Molecular Cloud Collapse and Fragmentation. *Astrophysical Journal*, 495:821, March 1998.

J. P. Williams, L. Blitz, and A. A. Stark. The Density Structure in the Rosette Molecular Cloud: Signposts of Evolution. *Astrophysical Journal*, 451:252, September 1995.